

1 **Improved constraints on northern extratropical CO₂**
 2 **fluxes obtained by combining surface-based and**
 3 **space-based atmospheric CO₂ measurements**

4 **B. Byrne¹, J. Liu², M. Lee², I. Baker³, K. W. Bowman², N. M. Deutscher⁴,**
 5 **D. G. Feist⁵, D. W. T. Griffith⁴, L. T. Iraci⁶, M. Kiel², J. S. Kimball⁷,**
 6 **C. E. Miller², I. Morino⁸, N. C. Parazoo², C. Petri⁹, C. M. Roehl¹⁰,**
 7 **M. K. Sha¹¹, K. Strong¹², V. A. Velazco⁴, P. O. Wennberg^{10,13}, D. Wunch¹²**

8 ¹NASA Postdoctoral Program Fellow, Jet Propulsion Laboratory, California Institute of Technology, CA,
 9 USA

10 ²Jet Propulsion Laboratory, California Institute of Technology, CA, USA

11 ³Atmospheric Science Department, Colorado State University, Fort Collins, CO, USA

12 ⁴Centre for Atmospheric Chemistry, University of Wollongong, Wollongong, Australia

13 ⁵Max Planck Institute for Biogeochemistry, Jena, Germany

14 ⁶Atmospheric Science Branch, NASA Ames Research Center, Moffett Field, CA 94035, USA

15 ⁷Numerical Terradynamic Simulation Group, W.A. Franke College of Forestry & Conservation, The
 16 University of Montana, Missoula, MT 59812, USA

17 ⁸Satellite Observation Center, Center for Global Environmental Research, National Institute for
 18 Environmental Studies (NIES), 16-2 Onogawa, Tsukuba, Ibaraki 305-8506, Japan

19 ⁹Institute of Environmental Physics, University of Bremen, Bremen, Germany

20 ¹⁰Division of Geological and Planetary Sciences, California Institute of Technology, Pasadena, CA, USA

21 ¹¹Royal Belgian Institute for Space Aeronomy (BIRA-IASB), Brussels, Belgium

22 ¹²Department of Physics, University of Toronto, Toronto, Ontario, Canada

23 ¹³Division of Engineering and Applied Science, California Institute of Technology, Pasadena, CA, USA

24 ©2019. All rights reserved. California Institute of Technology, government spon-
 25 sorship acknowledged.

26 **Key Points:**

- 27 • Consistent flux constraints provided by surface in situ and flask, TCCON, and GOSAT
 28 measurements of atmospheric CO₂.
 29 • Combining data sets improves agreement between modeled and measured aircraft-
 30 based CO₂ measurements.
 31 • Improvements in NASA ACOS retrieval explain improved consistency of space-
 32 based and surface-based CO₂.

Corresponding author: Brendan Byrne, brendan.k.byrne@jpl.nasa.gov

33 **Abstract**

34 Top-down estimates of CO₂ fluxes are typically constrained by either surface-based or
 35 space-based CO₂ observations. Both of these measurement types have spatial and tem-
 36 poral gaps in observational coverage that can lead to biases in inferred fluxes. Assim-
 37 ilating both surface-based and space-based measurements concurrently in a flux inver-
 38 sion framework improves observational coverage and reduces sampling biases. This study
 39 examines the consistency of flux constraints provided by these different observations and
 40 the potential to combine them by performing a series of six-year (2010–2015) CO₂ flux
 41 inversions. Flux inversions are performed assimilating surface-based measurements from
 42 the in situ and flask network, measurements from the Total Carbon Column Observing
 43 Network (TCCON), and space-based measurements from the Greenhouse Gases Observ-
 44 ing Satellite (GOSAT), or all three datasets combined. Combining the datasets results
 45 in more precise flux estimates for sub-continental regions relative to any of the datasets
 46 alone. Combining the datasets also improves the accuracy of the posterior fluxes, based
 47 on reduced root-mean-square differences between posterior-flux-simulated CO₂ and aircraft-
 48 based CO₂ over midlatitude regions (0.35–0.50 ppm) in comparison to GOSAT (0.39–
 49 0.57 ppm), TCCON (0.52–0.63 ppm), or in situ and flask measurements (0.45–0.53 ppm)
 50 alone. These results suggest that surface-based and GOSAT measurements give comple-
 51 mentary constraints on CO₂ fluxes in the northern extratropics and can be combined
 52 in flux inversions to improve observational coverage. This stands in contrast with many
 53 earlier attempts to combine these datasets and suggests that improvements in the NASA
 54 Atmospheric CO₂ Observations from Space (ACOS) retrieval algorithm have significantly
 55 improved the consistency of space-based and surface-based flux constraints.

56 **1 Introduction**

57 Observations of atmospheric CO₂ provide a constraint on the net surface–atmosphere
 58 CO₂ flux, and are critical for monitoring carbon flux changes. This has motivated ob-
 59 servational programs that measure atmospheric CO₂, including a global network of surface-
 60 based in situ and flask monitoring sites, the Total Carbon Column Observing Network
 61 (TCCON) of ground-based spectrometers (Wunch et al., 2011) and several satellite mis-
 62 sions (Crisp et al., 2004; Yokota et al., 2009). These observations have provided many
 63 insights into the terrestrial carbon cycle (Keeling, 1960; Bolin & Keeling, 1963; Bacas-
 64 tow, 1976; Tans et al., 1989; Keeling et al., 1996; Bowman et al., 2017; J. Liu et al., 2017;
 65 Chatterjee et al., 2017). However, current measurement programs are unable to contin-
 66 uously monitor CO₂ with global coverage, resulting in observational gaps. These spa-
 67 tial and temporal gaps in observations of atmospheric CO₂ can introduce artifacts into
 68 NEE estimates, leading to difficulties in constraining carbon fluxes on regional scales (J. Liu
 69 et al., 2014; Byrne et al., 2017; Basu et al., 2018).

70 Different observing systems have different gaps in the observational coverage. Space-
 71 based measurements retrieve atmospheric CO₂ from measurements of reflected sunlight.
 72 This results in highly seasonal observational coverage in extratropical regions. Seasonal
 73 differences in observational coverage are further exasperated by challenging retrievals over
 74 snow (Nassar et al., 2014), and seasonal variations in cloud cover. In contrast, surface-
 75 based measurements of atmospheric CO₂ typically have comparatively uniform tempo-
 76 ral coverage, but poor spatial coverage. Surface measurements sites most densely cover
 77 the northern extratropics (particularly North America and Europe) but have sparse cov-
 78 erage elsewhere (Byrne et al., 2017).

79 In the northern extratropics, surface-based and space-based atmospheric CO₂ mea-
 80 surements provide complementary observational coverage in space and time, respectively.
 81 Yet, few studies have attempted to combine surface-based and space-based atmospheric
 82 CO₂ measurements to obtain top down constraints on fluxes across the northern lati-
 83 tudes. Chevallier et al. (2011) found consistency between the surface-air-sample-based

84 and the TCCON-based inversions, suggesting that flux inversions combining both data
 85 sources could be performed. Houweling et al. (2015) performed a series of CO₂ flux in-
 86 versions assimilating measurements from the Greenhouse Gases Observing Satellite (GOSAT)
 87 and surface-based CO₂ measurements. They found that comparisons between posterior
 88 CO₂ fields and aircraft data did not show significant differences between inversions as-
 89 similating surface-based or space-based measurements, and that the largest differences
 90 were driven by the inversion set up. However, they also found that the two datasets gave
 91 large differences in the spatial distribution of the CO₂ sink, with GOSAT flux inversions
 92 having increased uptake in the northern extratropics by ~1 PgC. When both datasets
 93 were combined, they found that the posterior fluxes did not recover the observed merid-
 94 ional gradient in CO₂ (which was also found for the GOSAT flux inversions), suggest-
 95 ing that the biases in retrieved GOSAT X_{CO₂} could be adversely impacting the results.
 96 Another study, Wang et al. (2018), assimilated both GOSAT measurements and surface-
 97 based atmospheric CO₂ measurements in a batch Bayesian synthesis inversion. They found
 98 that the differences in observational coverage of the ground-based and space-based datasets
 99 were complementary, resulting in smaller posterior uncertainty estimates when both datasets
 100 are assimilated than either dataset alone. Similarly, in a set of regional Observing Sys-
 101 tem Simulation Experiments (OSSEs), Fischer et al. (2017) showed reduced uncertainty
 102 in biosphere and fossil fuel emissions in California by combining space-based X_{CO₂} and
 103 surface-based flask and in situ measurements.

104 In this study, we further investigate combining ground-based and space-based mea-
 105 surements of atmospheric CO₂ to provide estimates of NEE globally, but we focus on north-
 106 ern extra-tropical regions where surface-based and aircraft-based measurements are most
 107 densely concentrated. We perform a series of six-year flux inversions (2010–2015, inclu-
 108 sive) assimilating surface-based measurements from the in situ and flask measurement
 109 network, TCCON column-averaged dry-air CO₂ mole fractions (X_{CO₂}), GOSAT X_{CO₂}
 110 measurements, and all three datasets combined. For each set of measurements, we per-
 111 form three flux inversions applying different prior NEE flux and error constraints. From
 112 the spread in posterior fluxes due to prior constraints, we quantify the precision to which
 113 these datasets constrain posterior fluxes. Spatial structures in the posterior fluxes are
 114 examined through comparisons between posterior-NEE-simulated X_{CO₂} and Orbiting
 115 Carbon Observatory 2 (OCO-2) X_{CO₂} measurements and the accuracy of posterior-NEE-
 116 simulated CO₂ is examined through comparisons with aircraft-based CO₂ measurements.

117 The paper is outlined as follows. Section 2 describes the measurements used in this
 118 study and Sec. 3 describes the flux inversion set-up. The posterior CO₂ fields obtained
 119 by the flux inversions are compared with OCO-2 and aircraft-based measurements in Sec. 4.1.
 120 We then examine the six-year-mean seasonal cycle and annual net fluxes (Sec. 4.2) and
 121 interannual variability (Sec. 4.3) obtained by the flux inversions. Finally, the implica-
 122 tions of the results are discussed in Sec. 5 and conclusions are given in Sec. 6.

123 2 Data

124 2.1 Surface-based in situ and flask measurements

125 Surface-based measurements of boundary layer atmospheric CO₂ can be performed
 126 using an in situ gas analyzer or by taking a flask sample, which is then returned to a lab
 127 and analyzed. A number of different groups from around the world collect surface CO₂
 128 observations. We assimilate measurements from version 4.1 of the GLOBALVIEW plus
 129 package (Masarie et al., 2014; Cooperative Global Atmospheric Data Integration Project,
 130 2018) and the Japan-Russia Siberian Tall Tower Inland Observation Network (JR-STATION)
 131 of nine tower sites in Siberia (Sasakawa et al., 2010, 2013).

132 The GLOBALVIEW v4.1 package incorporates data from many observing sites around
 133 the world and is specifically prepared for use in data assimilation studies. We include

134 measurements from the Integrated Carbon Observation System (ICOS RI, 2019) in our
 135 analysis. We assimilate GLOBALVIEW v4.1 measurements from surface in situ and flask
 136 sites, tower sites, and ship-based measurements. Data is only assimilated if the measure-
 137 ments are assimilated by NOAA’s CarbonTracker, version CT2017 (CT_assim = 0). Mea-
 138 surements are assimilated at the intake height above the model surface over land, and
 139 at the intake height above sea level for ocean grid cells. For surface-based flask and in situ
 140 measurements, most of the measurement error applied for assimilation is due to repre-
 141 sentativeness errors (inability to model these measurements). We use the model-data-
 142 mismatch (mdm) as the measurement errors. This is the error value placed on each mea-
 143 surement in the assimilation system, and is meant to express the statistics of simulated-
 144 minus-observed CO₂ residuals expected if CarbonTracker were using perfect surface fluxes.

145 JR-STATION is a network of nine towers (<http://www.cger.nies.go.jp/en/climate/pj1/tower/>).
 146 On these towers, high inlet measurements are obtained over the 17–20th minutes of each
 147 hour and the low inlet data is obtained from 37–40th minutes of each hour, these 3-minute
 148 averages are the taken to be representative of the hourly means for each inlet. We fil-
 149 ter the measurements by removing all measurements where the vertical gradient in CO₂
 150 exceeds 0.5 ppm (to remove measurements when the boundary layer is not well-mixed),
 151 and use the measured value at the highest intake for the measurement. For each site the
 152 errors (in ppm) are prescribed to be constant throughout a given month, the errors are
 153 the errors range from 3 ppm in winter to 7 ppm in summer, to account for both mea-
 154 surement and representativeness errors. These error estimates were chosen because they
 155 are comparable to the error estimates for tower sites in the GLOBALVIEW plus v4.1
 156 package.

157 We remove outliers and poorly modeled measurements by filtering out measure-
 158 ments for which the difference between the prior-NEE-simulated measurements and ac-
 159 tual measurements exceeds three standard deviations of the measurement uncertainty
 160 (See Sec. 3 for details on the forward model simulations). We also remove measurements
 161 for which the difference between prior simulated CO₂ and measurement exceeds 10 ppm,
 162 as these are assumed to be poorly simulated by the model. This filtering removes ~8%
 163 of the measurements. For each site, the data is only assimilated between 11 a.m. and
 164 4 p.m. local time.

165 **2.2 Aircraft-based measurements**

166 Aircraft measurements are used for the evaluation of posterior atmospheric CO₂
 167 fields. Aircraft data are obtained from the version 4.1 of the GLOBALVIEW plus dataset.
 168 Comparisons between measured and modeled atmospheric CO₂ are performed over three
 169 distinct regions: East Asia, North America, and Alaska/Arctic (Fig. S1). Aircraft mea-
 170 surements over East Asia come exclusively from the Comprehensive Observation Net-
 171 work for Trace gases by Airliner (CONTRAIL) program (Machida et al., 2008, 2018).
 172 Aircraft data over Alaska/Arctic and North America originate from the NOAA Global
 173 Greenhouse Gas Reference Network’s aircraft program (Sweeney et al., 2015) and HI-
 174 APER Pole-to-Pole Observations (HIPPO) (Wofsy, 2011). The number of hourly-mean
 175 measurements per month between 3–8 km in altitude above sea level (asl) are shown in
 176 Fig. S2.

177 **2.3 TCCON measurements**

178 TCCON is a network of ground-based Fourier transform spectrometers that record
 179 solar absorption spectra in the near-infrared from which, among other gases, X_{CO₂} is es-
 180 timated (Wunch et al., 2011). CO₂ abundances are retrieved using a non-linear least squares
 181 approach from absorption lines in the near-infrared spectral region. The column-averaged
 182 dry-air mole fractions of CO₂ (X_{CO₂}) is calculated by taking the ratio of the column abun-
 183 dance of CO₂ to O₂ (scaled by the mean O₂ concentration), resulting in high precision

Table 1. TCCON sites used in this study.

Site Name	Lat	Lon	Start Date	Reference
Eureka	80.05 N	86.42 W	25 Jul 2010	Strong et al. (2017)
Orleans	47.97 N	2.11 E	29 Aug 2009	Warneke et al. (2017)
Park Falls	45.95 N	90.27 W	02 Jun 2004	Wennberg, Roehl, et al. (2017)
Rikubetsu	43.46 N	143.77 E	16 Nov 2013	Morino et al. (2017)
Lamont	36.60 N	97.49 W	06 Jul 2008	Wennberg, Wunch, et al. (2017)
Edwards	34.96 N	117.88 W	20 Jul 2013	Iraci et al. (2017)
Ascension Island	7.92 S	14.33 W	22 May 2012	Feist et al. (2017)
Darwin	12.46 S	130.93 E	28 Aug 2005	Griffith, Deutscher, et al. (2017)
Reunion Island	20.90 S	55.49 E	16 Sep 2011	De Mazière et al. (2017)
Wollongong	34.41 S	150.88 E	26 Jun 2008	Griffith, Velazco, et al. (2017)

184 (<0.25% in CO₂) X_{CO₂} measurements. The TCCON strives to achieve the best site-to-
 185 site precision and accuracy possible. Systematic biases that are consistent throughout
 186 the network are fully accounted for by scaling the TCCON retrieval results to the WMO
 187 scale via aircraft and AirCore profiles (Wunch et al., 2010). Moreover, the TCCON sets
 188 guidelines to ensure that the instrumentation at each site is as similar as possible, and
 189 that the retrieval software, including the spectroscopic line lists and line shapes, is iden-
 190 tical for each site. However, site-specific differences (e.g. instrumental line shape) can
 191 cause residual site-to-site biases (Wunch et al., 2010) which might introduce biases in
 192 flux inversions.

193 For this study, TCCON data were obtained from the TCCON Data Archive, hosted
 194 by CaltechDATA [https://tccondata.org]. We include data from TCCON sites that have
 195 mean biases of less than 0.5 ppm relative to both the OCO-2 target-mode X_{CO₂} and the
 196 posterior-simulated X_{CO₂} from the surface-only flux inversions. The sites included in this
 197 study, which provide data during the years 2010–2015, are given in Table 1. Sites that
 198 are excluded from this study are excluded due to several factors that cause apparent bi-
 199 ases to be greater than 0.5 ppm. These factors include: proximity to large CO₂ sources
 200 (e.g., cities), proximity to large topographic variability, and in a few cases, known TC-
 201 CON instrument biases for which a solution either has been applied, or will be applied
 202 in an upcoming TCCON data version. Note that the threshold of 0.5 ppm is somewhat
 203 arbitrary. This value was set because most sites outside of this threshold are in heav-
 204 ily observed regions (e.g., Europe), which are expected to be well constrained by other
 205 datasets (Byrne et al., 2017), or in the Southern Hemisphere and not expected to have
 206 a large impact on the performance of the flux inversions in the northern mid-latitudes.

207 In this study, the TCCON data are filtered to remove measurements with solar zenith
 208 angles greater than 70 degrees. Measurements are then binned into hourly medians for
 209 each site. Only hours with five or more measurements are included. Measurements are
 210 only assimilated between 11am–3pm local time for the flux inversions, to minimize po-
 211 tential biases relating to errors in the prescribed diurnal cycle of NEE.

212 2.4 Space-based measurements

213 We assimilate X_{CO₂} measured by the Thermal And Near-infrared Sensor for car-
 214 bon Observations Fourier Transform Spectrometer (TANSO-FTS) aboard GOSAT. GOSAT
 215 was launched in February 2009 in a sun-synchronous orbit, with a repeat cycle of 3 days
 216 that produces 44 separate ground track repeats (Yoshida et al., 2013). The footprint of
 217 the GOSAT measurements has a diameter of about 10 km. Since August 2010, TANSO-
 218 FTS has been measuring with a 3-point cross-track pattern with 263 km cross track sep-
 219 aration, resulting in a swath of 526 km. Measurements have an along-track separation

220 of 283 km (Crisp et al., 2012). We use version 7.3 of the NASA Atmospheric CO₂ Ob-
 221 servations from Space (ACOS) GOSAT measurements in this analysis. A detailed de-
 222 scription of ACOS retrieval algorithm is available in O’Dell et al. (2012) and Crisp et al.
 223 (2012), with recent updates described in Eldering et al. (2017) and O’Dell et al. (2018).
 224 We assimilate all high gain (H-Gain) nadir measurements from the TANSO-FTS short-
 225 wave infrared (SWIR) band that pass the quality flag requirement.

226 Measurements from OCO-2 are used for comparisons with the posterior CO₂ fields.
 227 OCO-2, launched in July 2014, is a space-based spectrometer in a Sun-synchronous or-
 228 bit that measures reflected solar radiation to infer X_{CO₂} with a footprint of about 3 km².
 229 It has a repeat cycle of 16 days, resulting in 233 separate ground track repeats. OCO-
 230 2 has a swath of 10 km and collects eight adjacent, spatially resolved samples every 0.333 s,
 231 resulting in roughly 24 soundings per second. We downloaded version 9 of the ACOS OCO-
 232 2 lite files from the CO₂ Virtual Science Data Environment (<https://co2.jpl.nasa.gov/>).
 233 Measurements are averaged into super-obs at 1° × 1° resolution grids following J. Liu
 234 et al. (2017), with the additional requirement that there must be a minimum of eight
 235 OCO-2 observations within each 1° × 1° gridbox. We combine land nadir and land glint
 236 measurements for the analysis.

237 3 Flux inversions

238 Flux inversions are performed with the Greenhouse Gas Framework – Flux (GHGF-
 239 Flux) inversion system. GHGF-Flux is a flux inversion system developed under the NASA’s
 240 Carbon Monitoring System (CMS) project. The GHGF is capable of jointly assimilating
 241 multi-platform observations of CH₄, CO, CO₂, and OCS. The GHGF inherits the
 242 chemistry transport model from the GEOS-Chem and the adjoint analysis methods from
 243 the GEOS-Chem-adjoint.

244 Chemical transport is driven by the Modern-Era Retrospective Analysis for Re-
 245 search and Applications, Version 2 (MERRA-2) meteorology produced with version 5.12.4
 246 of the GEOS atmospheric data assimilation system (Gelaro et al., 2017). To perform tracer
 247 transport, these fields are regridded to 4° × 5° horizontal resolution and archived with
 248 a temporal resolution of 6 h except for surface quantities and mixing depths, which have
 249 a temporal resolution of 3 h. Tracer transport is performed at 30 min time steps.

250 For all inversions, we optimize 14 day scaling factors for daily net NEE and ocean
 251 fluxes, except for the final temporal grouping of each year, which is padded with 1–2 days
 252 so that the groupings cover the same day-of-year increments for each year. We use an
 253 assimilation window of approximately 18 months (October 7 to April 1 two years later)
 254 and keep posterior fluxes for one year (Jan 1 to Dec 31) then shift the inversion window
 255 forward one year. Using this method, we optimize NEE spanning 2010–2015. Initial con-
 256 ditions are generated by performing a two year inversion of surface in situ and flask mea-
 257 surements spanning 1 Jan 2008 to 31 Dec 2009. The stratosphere is then adjusted to match
 258 the zonal mean structure of Diallo et al. (2017) for October 2009 (adjusted by a few parts
 259 per million).

260 Prior NEE fluxes and errors differ between inversions, and are generated from three
 261 different models: the Simple Biosphere model (SiB3), the Carnegie-Ames-Stanford Ap-
 262 proach model (CASA) and FLUXCOM. The motivation for using three different priors
 263 is that the posterior flux estimates may be sensitive to prior fluxes (Philip et al., 2019),
 264 thus using an ensemble of prior flux estimates provides an estimate of the precision to
 265 which the observations constrain fluxes. For all prior fluxes the annual total net flux has
 266 been adjusted to 4.6 PgC yr⁻¹, to match the mean atmospheric CO₂ growth rate. De-
 267 tails on the modeled NEE fluxes and prior errors are given in Appendix 7. The diurnal
 268 cycle in NEE is prescribed using the modeled diurnal cycle from SiB3 for the SiB3 flux
 269 inversions and the diurnal cycle from CASA for the CASA and FLUXCOM inversions.

270 Sensitivity tests found that the flux inversions were not sensitive to the prescribed di-
 271 urnal NEE cycle. The ECCO-Darwin-V1 model (Menemenlis et al., 2008; Dutkiewicz
 272 et al., 2009; Brix et al., 2015) estimates are used as the prior ocean CO₂ exchange for
 273 all inversions, and prior errors were taken to be 100% of the flux. Fossil fuel, biofuel, and
 274 biomass burning CO₂ emissions are prescribed using the Open-source Data Inventory
 275 for Anthropogenic CO₂, version 2018 (Oda & Maksyutov, 2011; Oda et al., 2018) with
 276 downscaling to hourly emissions based on Nassar et al. (2013), CASA-GFED4-FUEL,
 277 and Global Fire Emission Database, version 4 (GFED4) (Randerson et al., 2018) inven-
 278 tories, respectively.

279 Prior error covariance matrices are taken to be diagonal, such that there are no spa-
 280 tial or temporal covariances. The prior NEE errors are generated based on the NEE fluxes
 281 provided by the models. It is first taken to be 60% of the NEE flux. This is then increased
 282 by scaling up the errors at times and grid cells that have active vegetation but small net
 283 fluxes. For example, the uncertainty is scaled up during the spring (source to sink) and
 284 fall (sink to source) transition periods when the 14-day NEE flux is small but the sum-
 285 mer 14-day NEE fluxes are much larger. We also inflate the uncertainty for gridcells in
 286 which the flux is small for a given model but is much larger for the other models. The
 287 final errors range from 100% to 500% of the NEE flux. Additional details are provided
 288 in Appendix 7.

289 A series of flux inversions are performed that assimilate different datasets. This al-
 290 lows us to quantify the influence of different observational datasets on the posterior fluxes.
 291 We perform flux inversions that assimilate only ground-based in situ and flask measure-
 292 ments (referred to as surface-only), only TCCON measurements (TCCON-only), only
 293 GOSAT data (referred to as GOSAT-only), and all datasets simultaneously (referred to
 294 as GOSAT+surface+TCCON). For each data assimilation set-up, we perform flux in-
 295 versions with each of the three prior NEE fluxes and errors. Therefore, we perform a to-
 296 tal of 12 flux inversions.

297 4 Results

298 4.1 Evaluation of posterior-NEE-simulated CO₂

299 Large spatial structures in the posterior-simulated-CO₂ fields are compared with
 300 GOSAT and OCO-2 X_{CO₂}, while the accuracy of the fluxes are evaluated against aircraft-
 301 based CO₂ measurements. Rather than describing the data–model differences for all 12
 302 inversions, the posterior fluxes are grouped by the dataset assimilated and the mean pos-
 303 terior fluxes are evaluated. Tables giving the data–model mismatch between the indi-
 304 vidual flux inversions and aircraft measurements are provided as supplementary materi-
 305 als (Tables SS1 and SS2).

306 4.1.1 Comparison of posterior CO₂ against space-based X_{CO₂}

307 Space-based X_{CO₂} measurements have broad spatial coverage on the timescale of
 308 a month. This allows for comparisons between modeled and measured X_{CO₂} data over
 309 large spatial scales. Here, the data–model mismatch between the posterior CO₂ fields
 310 and space-based measurements from GOSAT and OCO-2 are examined. Figure 1 shows
 311 the zonal mean data–model mismatch as a function of latitude and time for the mean
 312 prior fluxes and mean posterior fluxes for the TCCON-only inversions, surface-only in-
 313 versions, GOSAT-only inversions, and GOSAT+surface+TCCON inversions. Note that
 314 there are gaps due to GOSAT’s observational coverage in the tropics and at high lati-
 315 tudes. The mean prior flux gives larger data–model standard deviations against GOSAT
 316 (0.59 ppm) and OCO-2 (0.67 ppm) than all of the flux inversions, implying that the flux
 317 inversions improve the variance of the data–model mismatch. The CO₂ fields simulated
 318 with the prior fluxes tend to be biased low relative to GOSAT and OCO-2 during the

319 winter and spring and biased high during the summer and fall in the northern extratropics, suggesting that the prior fluxes underestimate the magnitude of the seasonal cycle. Comparing the posterior CO₂ fields against GOSAT, the surface-only and TCCON-only flux inversions give the largest mean data–model standard deviations, which is expected as there were the only inversions that do not assimilate GOSAT data.

324 Comparing to OCO-2, all of the flux inversions give similar differences. Mean differences range from -0.11 ppm to 0.07 ppm and standard deviations range over 0.41-0.48 ppm, suggesting that all of the flux inversions recover the global X_{CO₂} fields with similar accuracy and precision. However, north of 40 °N, the GOSAT+surface+TCCON flux inversion shows better agreement with OCO-2 (RMS=0.30 ppm) than the other flux inversions (RMS=0.36–0.41 ppm). Differences between posterior-simulated X_{CO₂} and the OCO-2 measurements are largest in the northern subtropics, where the assimilated datasets have sparse observational coverage. Thus, it is unclear whether the differences in the subtropics are due to gaps in the observational coverage or biases in the OCO-2 retrievals.

333 The spread in simulated X_{CO₂} among the inversions gives a metric of the precision to which the flux inversion recovers atmospheric CO₂. Figure 2 shows the range of simulated GOSAT X_{CO₂} for the prior and posterior fluxes due to the different prior NEE fluxes and errors applied in the inversions. The largest range is obtained for the prior fluxes (mean of 1.37 ppm). The range for the TCCON-only and surface-only fluxes are reduced by 42% (0.79 ppm) and 64% (0.50 ppm) relative to the prior, respectively. However, for both flux inversions, most of the decrease in range occurs in the northern extratropics, where surface-based in situ, flask, and TCCON measurements are most concentrated. In contrast, the range increases in the tropics, where there is sparse observational coverage. This suggests that the tropical posterior NEE fluxes for the TCCON-only and surface-only flux inversions are highly sensitive to the prior NEE and error constraints. Globally, the range for GOSAT-only and GOSAT+surface+TCCON inversions are reduced by 72% and 78%, respectively, relative to the prior. The decrease relative to the prior is largest in the northern extratropics. Differences in range between the GOSAT-only and GOSAT+surface+TCCON inversions are generally quite small. The most notable difference is that the GOSAT+surface+TCCON inversions have a smaller range in the northern extratropics during the fall. GOSAT measurements do not have high sensitivity to northern extratropical fluxes during this time of year (Byrne et al., 2017), thus it appears that the surface-based measurements provide the additional information necessary to better constrain fall NEE in the northern extratropics.

353 ***4.1.2 Evaluation of posterior CO₂ against aircraft-based measurements***

354 Aircraft-based measurements of atmospheric CO₂ provide a constraint on atmospheric CO₂ that is independent of the surface-based and space-based datasets assimilated. Therefore, aircraft-based CO₂ measurements offer a dataset that modeled atmospheric CO₂ can be evaluated against. Here, we evaluate the atmospheric CO₂ fields simulated using the prior and posterior fluxes against aircraft measurements over three regions with intensive sampling: East Asia, North America, and Alaska/Arctic. We only use aircraft data between 3–8 km in altitude above sea level. Differences between measured and modeled CO₂ are due to both model transport errors and surface flux errors. We have found that the differences are strongly influenced by model transport errors for individual measurements but that the impact of representativeness errors on data–model mismatches is reduced with temporal aggregation, thus we aggregate data–model mismatches to monthly means.

366 The GOSAT+surface+TCCON flux inversions generally show the best agreement with the aircraft-based CO₂ measurements. Figure 3 shows the monthly-mean aircraft measurements and modeled CO₂ for the three regions examined here. The GOSAT+surface+TCCON flux inversions give the smallest RMS difference against aircraft-based CO₂ in East Asia

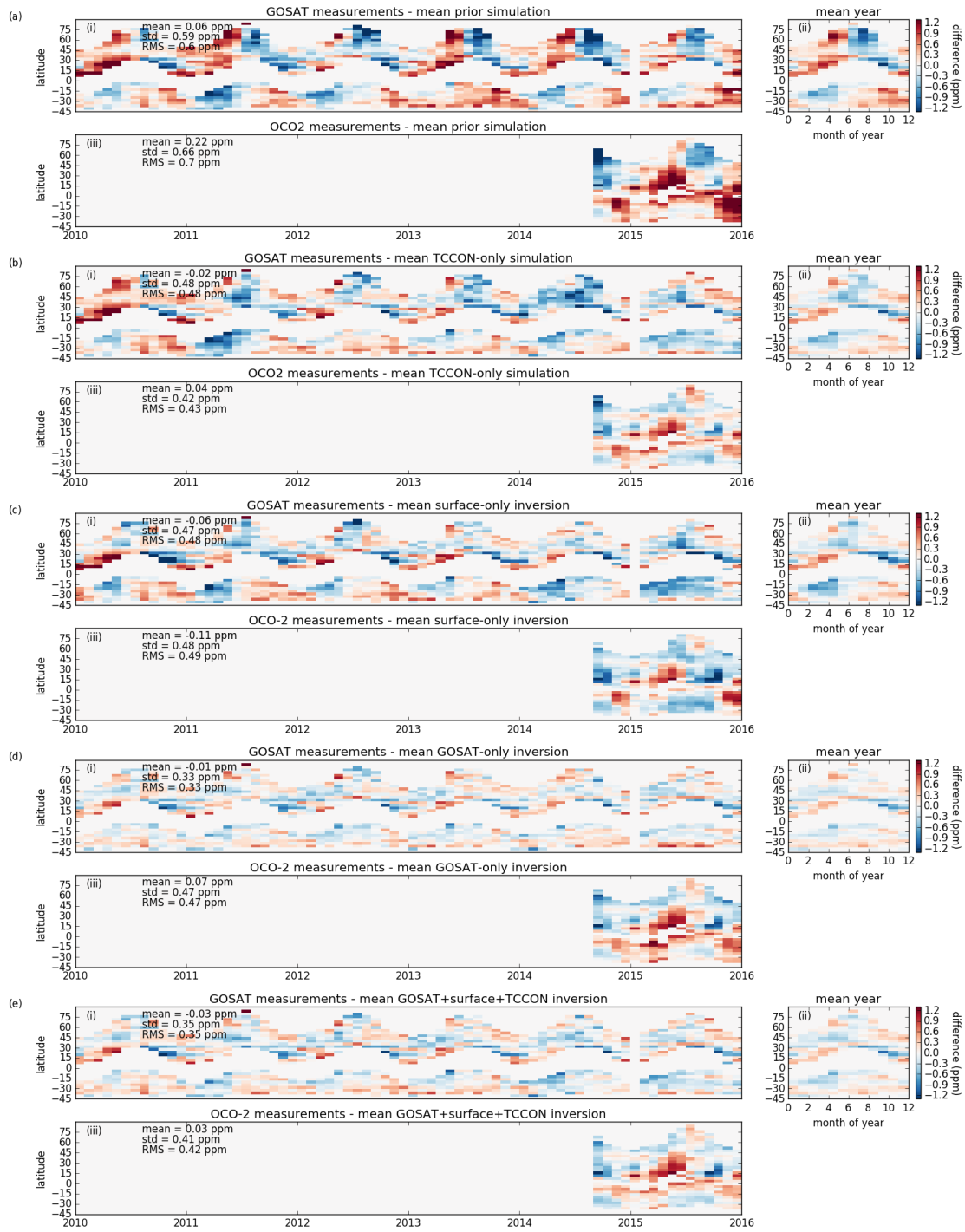


Figure 1. Zonal mean data-model mismatch for space-based X_{CO_2} measurements as a function of latitude and time for the (a) prior fluxes, (b) TCCON-only inversions (c) surface-only inversions, (d) GOSAT-only inversions, and (e) GOSAT+surface+TCCON inversions. For each set of flux inversions, the three panels show (i) the zonal and monthly mean GOSAT X_{CO_2} data-model difference for 2010 through 2015. (ii) The mean GOSAT X_{CO_2} data-model difference for each month of the year. (iii) The zonal and monthly mean OCO-2 X_{CO_2} data-model difference for 2014 through 2015.

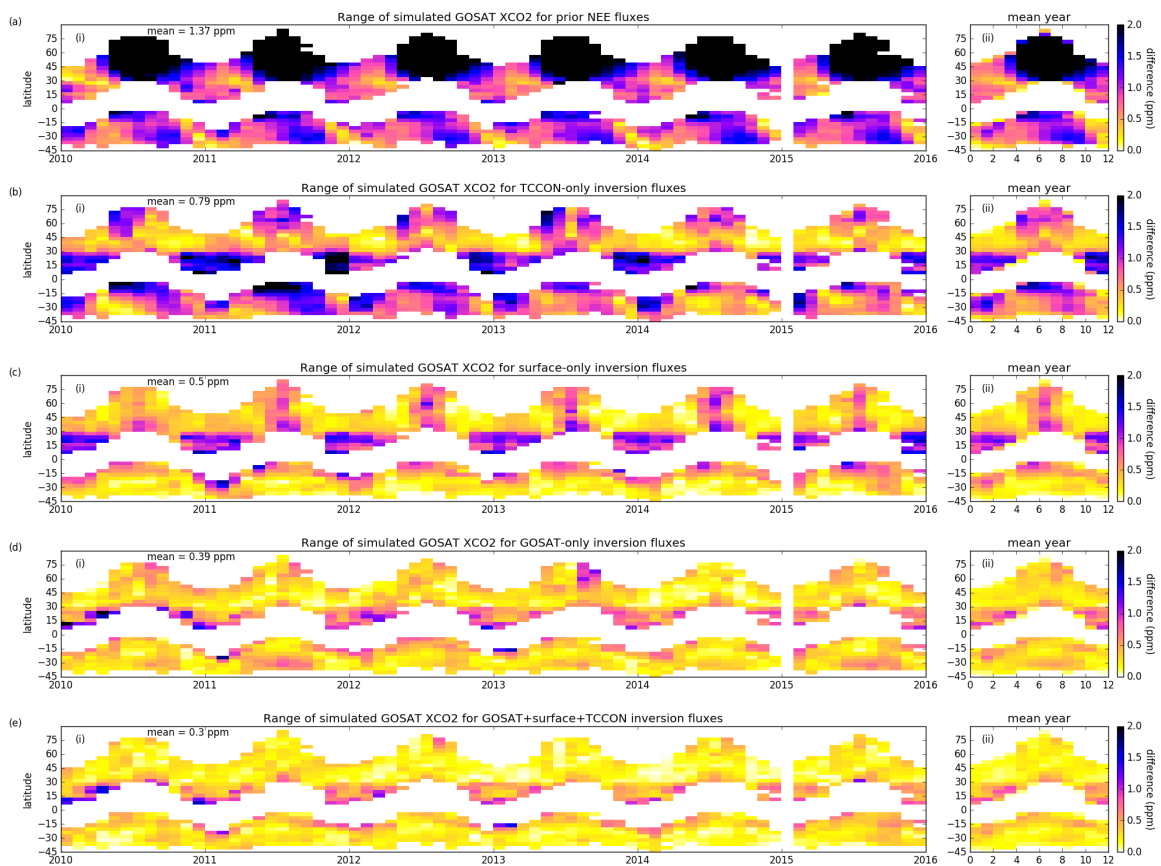


Figure 2. Spread in zonal and monthly mean simulated GOSAT X_{CO_2} for (a) prior NEE, (b) TCCON-only, (c) surface-only posterior NEE, (d) GOSAT-only posterior NEE, (e) GOSAT+surface+TCCON posterior NEE as a function of latitude and time. For each set of flux inversions sets, the panels show (i) the zonal and monthly mean range for 2010 through 2015, and (ii) The mean range for each month of the year.

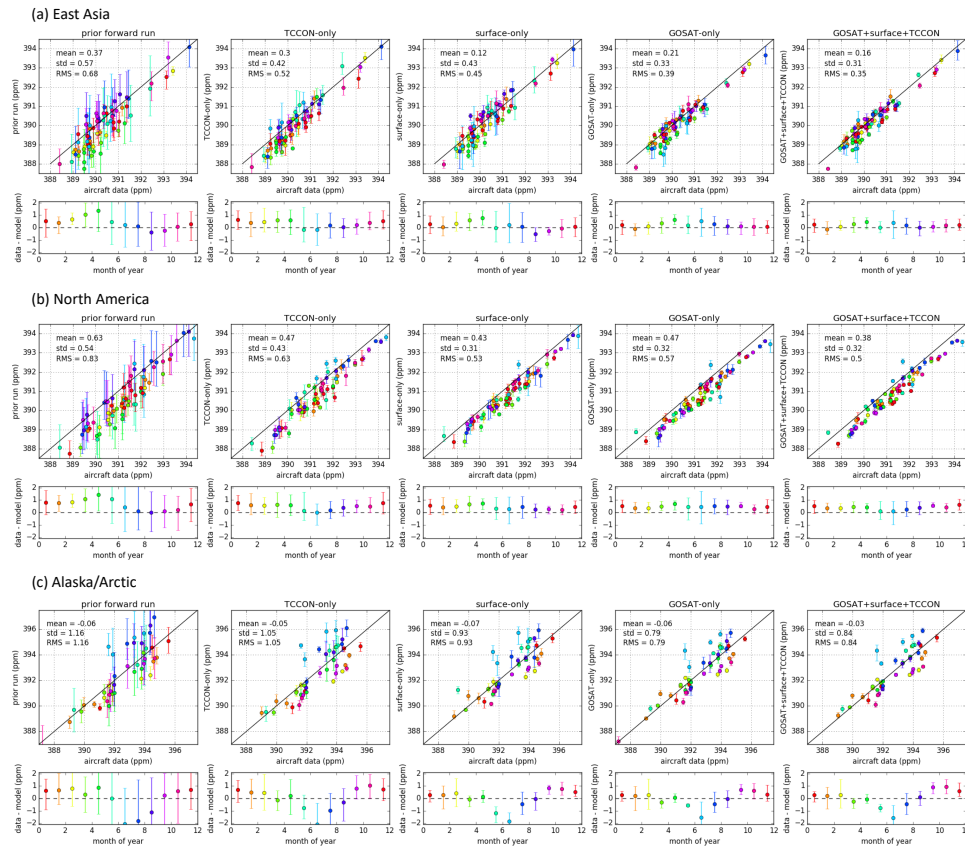


Figure 3. Comparison of monthly mean measured and simulated aircraft-based CO₂ for (a) East Asia, (b) North America, and (c) Alaska/Arctic. For each region, the mismatch for (left to right) prior, TCCON-only, surface-only, GOSAT-only, and GOSAT+surface+TCCON simulated CO₂ are shown. The top panel shows a scatter plot of the simulated aircraft-based CO₂ against the measured aircraft-based CO₂, and the error bars indicate the spread in posterior NEE. The lower panel shows the mean data–model mismatch for each month, with error bars showing the range of monthly mean mismatched over the six-years and inversion set-ups. Colors correspond to the month of year.

370 (0.35 ppm) and North America (0.50 ppm). The GOSAT-only flux inversions give the
 371 smallest RMS difference over the Alaska/Arctic region (0.79 ppm), although all of the
 372 flux inversions give larger RMS differences over this region relative to the midlatitude
 373 regions, suggesting that none of the flux inversions fully recover NEE at high latitudes.
 374 These aircraft measurements are also sensitive to fluxes over Siberia (Fig. S4), which is
 375 poorly observed by all datasets. Differences in the data–model mismatch between flux
 376 inversions are evident as a function of month-of-year. The GOSAT+surface+TCCON
 377 flux inversion tends to best capture month-to-month variability, while both flux in-
 378 versions assimilating GOSAT measurements tend to have less seasonality in the data–model
 379 mismatch than the TCCON-only and surface-only flux inversions. This is most evident
 380 for East Asia and suggests that the GOSAT-only flux inversions better capture the month-
 381 to-month variability in fluxes (consistent with the results of Polavarapu et al. (2018) and
 382 Byrne et al. (2019)).

383 Despite these differences, the data–model biases against the aircraft-based mea-
 384 surements are generally similar between flux inversions. For example, all of the flux in-

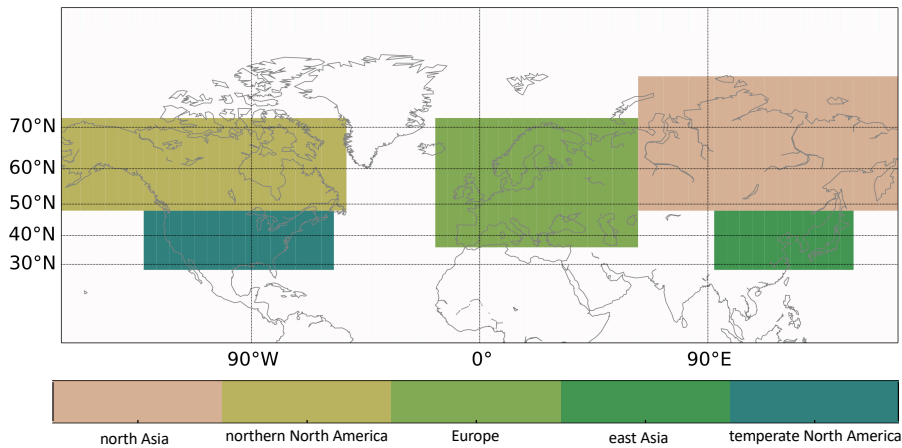


Figure 4. Five regions examined in this study. From left to right, the highlighted regions are referred to as northern North America, temperate North America, Europe, north Asia, and east Asia.

versions give positive biases for East Asia (0.12–0.30 ppm) and North America (0.38–0.47 ppm) but negative biases for the Alaska/Arctic region (-0.07 to -0.03 ppm). The fact that the data–model biases are similar suggests that these biases are sensitive to transport errors. This was quantified by regridding the fluxes and performing the evaluation against aircraft measurements at $2^\circ \times 2.5^\circ$ spatial resolution (Figure S3). We find that model-data biases for the flux inversions change by 0.01–0.03 ppm for East Asia, 0.07–0.10 ppm for North America, and 0.08–0.11 ppm for Alaska/Arctic. These differences are similar to the magnitude of data–model differences between flux inversions, suggesting that transport model errors limit the ability of evaluating CO₂ flux estimates with aircraft-based measurements.

4.2 Mean fluxes

4.2.1 Seasonal Cycle

In the northern extratropics, the seasonal cycle of NEE produces a large annual oscillation in atmospheric CO₂, giving seasonal variations of ~ 10 ppm in X_{CO₂}. This provides the largest signal of ecosystem carbon dynamics in atmospheric CO₂ and is the NEE signal that is best captured in CO₂ flux inversions. In this section, we examine the seasonal cycle of NEE recovered by the flux inversions in the northern extratropics grouped by the assimilated dataset. Figure 5 shows the seasonal cycle for the entire northern extratropics and five sub-continental regions (the spatial extent of the sub-continental regions are shown in Fig. 4). We examine (1) the consistency in the seasonal cycle between the datasets and (2) the precision of the posterior fluxes due to prior assumptions.

The posterior seasonal cycles of the flux inversions show consistent seasonal cycles for all assimilated datasets, relative to the prior fluxes. The GOSAT+surface+TCCON NEE fluxes most closely match the GOSAT-only NEE fluxes during the summer, as GOSAT has dense observational coverage. During the winter, the GOSAT+surface+TCCON NEE fluxes most closely match the surface-only fluxes, particularly over temperate North America and Europe where the surface-based measurements are most densely concentrated.

The spread for each set of flux inversions shows the range in posterior fluxes due to differences in the prior fluxes and errors applied. This provides a metric of the pre-

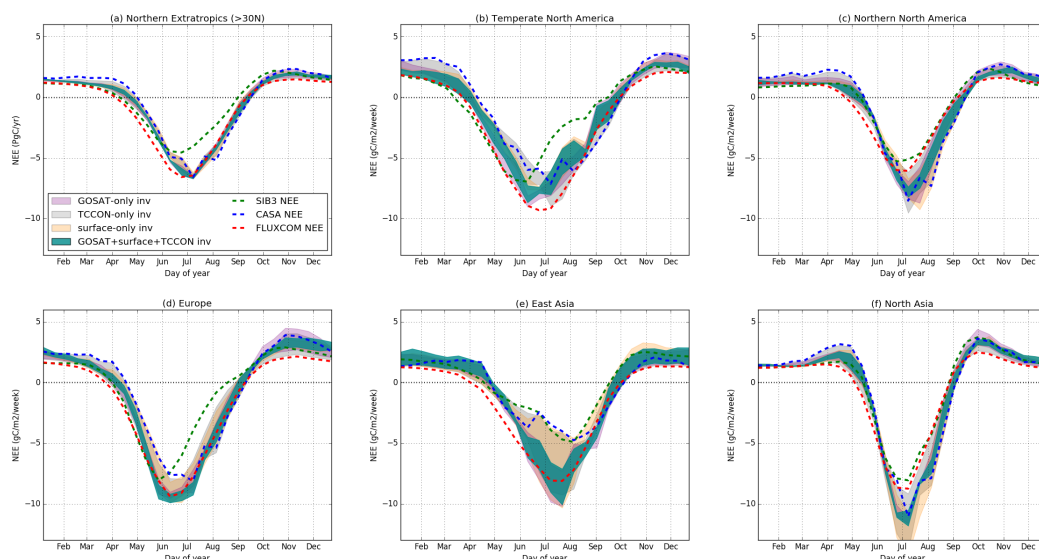


Figure 5. Prior and posterior NEE fluxes for (a) the entire northern extratropics ($\geq 30^\circ$ N), (b) temperate North America, (c) northern North America, (d) Europe, (e) east Asia, and (f) north Asia at 14 day temporal resolution. The shaded curves show the range of posterior fluxes obtained by the GOSAT-only (purple), TCCON-only (grey), surface-only (yellow), and GOSAT+surface+TCCON (dark green) flux inversions. Dashed lines show the seasonal cycles for the three prior NEE fluxes used in inversions: SiB3 (green), CASA (blue), and FLUXCOM (red).

414 precision to which the assimilated observations can constrain NEE. The spread is generally
 415 largest for the surface-only flux inversions outside of the winter. This is particularly no-
 416 table over East Asia, where there is comparatively sparse observational coverage lead-
 417 ing to a large spread among surface-only flux inversions. The spread is smallest for the
 418 GOSAT+surface+TCCON flux inversion, as expected. The small spread for the GOSAT+surface+TCCON
 419 flux inversions shows that the observational constraints provided by combining GOSAT,
 420 TCCON, and surface in situ and flask CO_2 measurements are sufficient to constrain the
 421 seasonal cycle of NEE on these sub-continental scales. These results suggest that the sea-
 422 sonal cycle is recovered by top-down flux inversions and suggests that analysis of the sea-
 423 sonal cycle of NEE, such as that presented by Byrne et al. (2018), could be extended to
 424 these regional scales.

4.2.2 Annual net fluxes

425
 426 Here, we examine the annual net fluxes obtained for the flux inversions over the
 427 northern extratropics. Figure 6 shows the six-year mean annual net fluxes for each sub-
 428 continental region. Over the entire northern extratropics ($>30^\circ$ N), the flux inversions
 429 show high consistency relative to the spread in the prior. We obtain a mean annual net
 430 flux of $-2.80 \text{ PgC yr}^{-1}$ (range of -3.43 to $-2.41 \text{ PgC yr}^{-1}$) for the TCCON-only flux
 431 inversions, $-2.76 \text{ PgC yr}^{-1}$ (range of -3.20 to $-2.49 \text{ PgC yr}^{-1}$) for the surface-only flux
 432 inversions, $-2.89 \text{ PgC yr}^{-1}$ (range of -3.31 to $-2.65 \text{ PgC yr}^{-1}$) for the GOSAT-only
 433 flux inversions, and $-3.02 \text{ PgC yr}^{-1}$ (range of -3.21 to $-2.89 \text{ PgC yr}^{-1}$) for the GOSAT+surface+TCCON
 434 flux inversions. It is notable that the prior assumptions applied to the flux inversions in-
 435 troduce substantial differences into the posterior fluxes. The range in the northern ex-
 436 tratropical sink due to applying different prior NEE fluxes and errors is $0.32\text{--}1.03 \text{ PgC yr}^{-1}$,
 437 depending on the assimilated dataset.

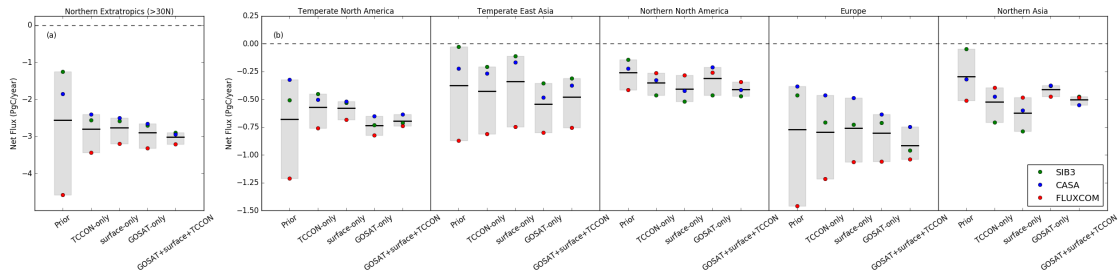


Figure 6. Six-year-mean annual net NEE fluxes for (a) all of the northern extratropics and (b) the five regions examined in this study. Shaded grey regions show the range for the prior and posterior fluxes, while the solid black line shows the mean. Individual inversions are shown by the filled circles, with colors indicating prior NEE applied: green circles indicate SiB3, blue circles indicate CASA, and red circles indicate FLUXCOM.

438 On regional scales, there is generally overlap in the range of net annual fluxes be-
 439 tween the TCCON-only, surface-only, GOSAT-only, and GOSAT+surface+TCCON flux
 440 inversions. This suggests that these observational datasets provide a consistent constraint
 441 on regional net annual NEE, within the considerable uncertainty introduced through prior
 442 assumptions. The exception is north Asia, where the surface-only inversions suggest a
 443 systematically larger sink than the GOSAT-only flux inversions. This region has poor
 444 observational coverage, which may explain the differences seen here.

445 **4.3 Interannual variability**

446 Interannual variability (IAV) in NEE provides a measure of the response of ecosys-
 447 tems to climate variability. Here, we examine the IAV recovered by the flux inversions,
 448 where IAV is calculated to be the anomaly from the six-year mean. Figure 7 shows the
 449 IAV in NEE for the entire northern extratropics and five extratropical regions at 14-day
 450 temporal resolution, after performing a 3-point (42-day) running mean to filter out high
 451 frequency variability. The posterior NEE IAV is not sensitive to the prior NEE constraints
 452 applied in the flux inversion, such that similar posterior NEE IAV is recovered for each
 453 set of prior fluxes when a given assimilated dataset. This is illustrated by the small range
 454 obtained for each set of colored curves. However, the posterior NEE IAV is sensitive to
 455 the assimilated dataset, such that we find disagreement in NEE IAV for the TCCON-
 456 only, surface-only, and GOSAT-only flux inversions.

457 Differences in IAV between flux inversions can partially be explained by differences
 458 in the observational coverage of the datasets. As an example, let's consider the differ-
 459 ences in IAV between the surface-only and GOSAT-only flux inversions in 2011 over tem-
 460 perate North America (Fig. 8). Figure 8a shows the monthly CO₂ anomalies observed
 461 by GOSAT and the surface in situ and flask network over the summer of 2011. GOSAT
 462 X_{CO₂} measurements are distributed uniformly across North America, while surface in situ
 463 and flask measurements are located south of Lake Superior. This observational cover-
 464 age is reflected in the posterior fluxes. The GOSAT-only posterior NEE anomalies (Fig. 8b)
 465 reflect the large scale structures in the X_{CO₂} anomalies but miss smaller scale structures,
 466 such as the positive anomalies over south central North America. The surface-only post-
 467 erior anomalies (Fig. 8c) capture large anomalies seen in CO₂, such as the anomalous
 468 release of CO₂ in south central North America, but miss much of the large scale struc-
 469 tures. Combining these two datasets in a single inversion, referred to as “GOSAT+surface”,
 470 captures both the large scale structures from the GOSAT-only and small-scale structures
 471 from the surface-only flux inversion (Fig. 8d). The posterior NEE anomalies from the

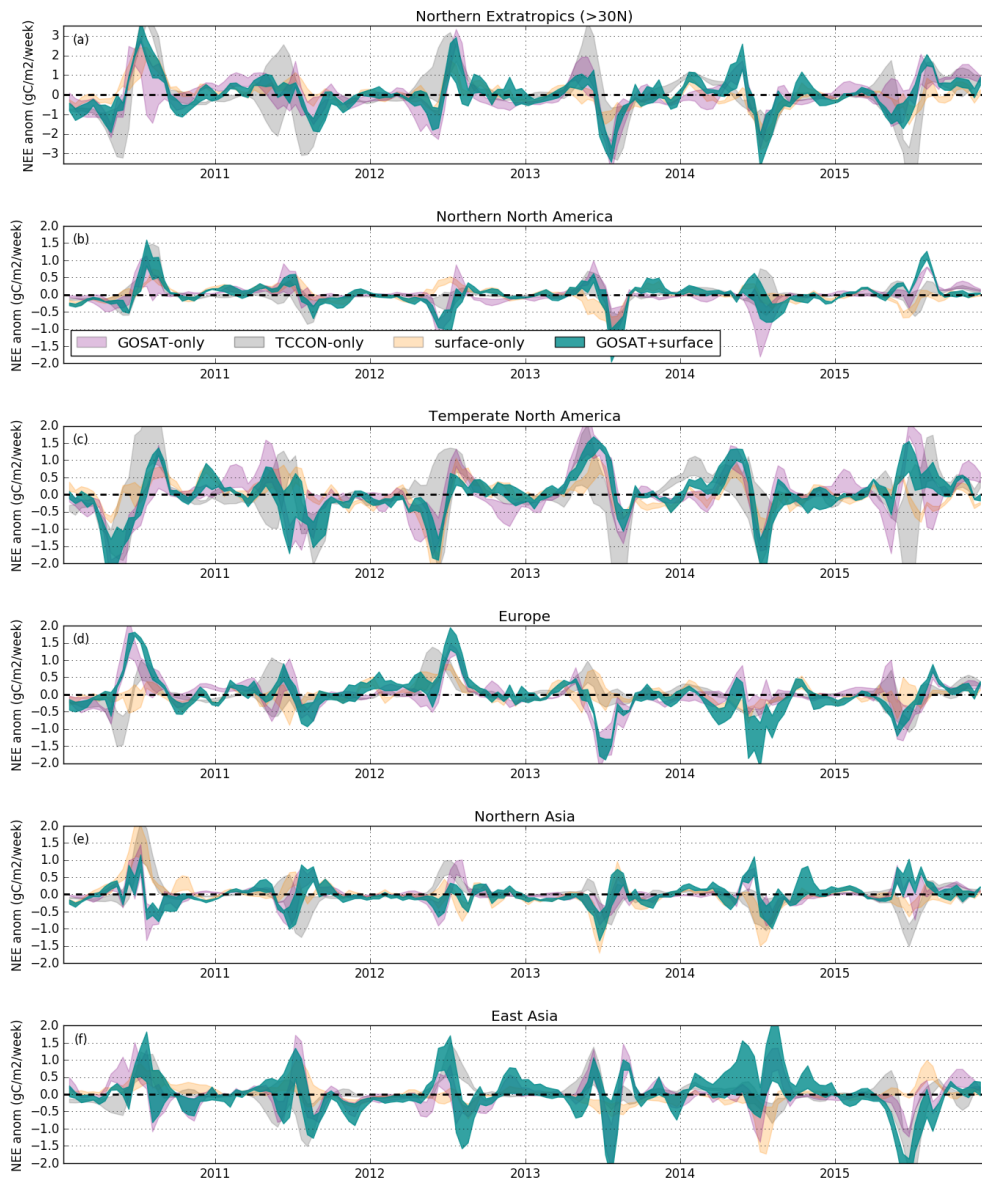


Figure 7. IAV in NEE for 2010–2015 at 14 day temporal resolution for (a) the entire northern extratropics ($\geq 30^\circ$ N), (b) temperate North America, (c) northern North America, (d) Europe, (e) east Asia, and (f) north Asia. The shaded curves show the range of posterior fluxes obtained by the GOSAT-only (purple), TCCON-only (grey), surface-only (yellow), and GOSAT+surface+TCCON (dark green) flux inversions. A 3-point (42 day) running mean is performed to remove high frequency variability.

472 GOSAT+surface flux inversion also correlate with anomalies in soil temperature (mean
473 of MERRA-2 soil temperature over levels 1–3, Reichle et al. (2011, 2017)) (Fig. 8e) and
474 soil moisture (ESA CCI Surface Soil Moisture Product, Y. Y. Liu et al. (2011, 2012); Wag-
475 ner et al. (2012); Gruber et al. (2017); Dorigo et al. (2017)) (Fig. 8f) over this time pe-
476 riod, suggesting that combining these datasets produces more realistic NEE IAV. Sim-
477 ilar results were found over Eurasia during the summer of 2010 (Fig. S5).

478 On an annual basis, we find mixed agreement between flux inversions in year-to-
479 year variations. Figure 9 shows IAV in annual net NEE anomalies for the entire north-
480 ern extratropics. In general, IAV in annual net fluxes are consistent for a given set of as-
481 similated data, suggesting that the results are not sensitive to the prior fluxes and er-
482 rors used. Note that the prior NEE fluxes did not contain IAV, which has previously been
483 shown to have a substantial impact on posterior NEE IAV (Byrne et al., 2019). How-
484 ever, posterior IAV is quite variable between different assimilated datasets. The cause
485 of these differences between the flux inversions are likely partially due to differences in
486 the observational coverage between datasets. It is possible that differences between datasets
487 are also partially due to changes in the observational coverage over time, which has pre-
488 viously been shown to have an impact on inferred fluxes (Rödenbeck et al., 2003; Gur-
489 ney et al., 2008; Bruhwiler et al., 2011).

490 5 Discussion

491 5.1 Consistency in surface-based and spaced-based flux constraints

492 The results generally show good agreement between the flux inversions assimilating
493 different datasets. The agreement between the surface-only and GOSAT-only flux
494 inversions may seem surprising in the context of a number of previous studies that have
495 shown substantial differences between surface-based and space-based flux estimates (Basu
496 et al., 2013; Chevallier et al., 2014; Houweling et al., 2015). However, more recent stud-
497 ies have shown improved agreement between surface-based and space-based flux inver-
498 sions. Chevallier et al. (2019) found that flux inversions assimilating OCO-2 ACOS ver-
499 sion 9 measurements gave similar net annual fluxes to those assimilating surface-based
500 measurements, and that both compared well against aircraft measurements. Interest-
501 ingly, Chevallier et al. (2019) also found that GOSAT OCO Full Physics (OCFP) v7.1
502 XCO₂ retrievals did not compare as well against aircraft measurements. Comparisons
503 between the ACOS 7.3 and OCFP v7.1 (downloaded from the Copernicus Climate Change
504 Service, <https://climate.copernicus.eu/>) show substantial differences in zonal mean XCO₂
505 (Fig. S6). Furthermore, GOSAT ACOS 7.3 retrievals are found to give better agreement
506 with posterior-simulated-CO₂ from the surface-only flux inversion (Fig. S7). This sug-
507 gests that the specific retrieval algorithm used has a large impact on the posterior fluxes,
508 such that the improved agreement between surface-based and space-based measurements
509 found in recent studies may be primarily due to improvements in the ACOS XCO₂ re-
510 trieval algorithm. Miller and Michalak (2019) have also argued that recent improvements
511 in the ACOS algorithm have substantially increased the reliability of OCO-2 XCO₂ mea-
512 surements in flux inversions studies (for version 8 in particular). Substantial work has
513 gone into refining the ACOS retrieval algorithm over the past decade (O’Dell et al., 2012;
514 Crisp et al., 2012; Eldering et al., 2017; O’Dell et al., 2018; Kiel et al., 2019; Nelson &
515 O’Dell, 2019). Thus, the improved agreement between surface-based and space-based CO₂
516 constraints is likely best explained by improvements in the ACOS retrieval algorithm.

517 A consistent six-year mean northern extratropical sink is obtained by all observa-
518 tional datasets. This result is in contrast to several previous studies that found substan-
519 tial differences in the annual net NEE flux of CO₂ in the northern extratropics between
520 flux inversions assimilating surface-based and space-based measurements (Basu et al.,
521 2013; Saeki et al., 2013; Chevallier et al., 2014; Reuter et al., 2014). The reason why we
522 obtain a more consistent annual net flux between datasets than some earlier studies is

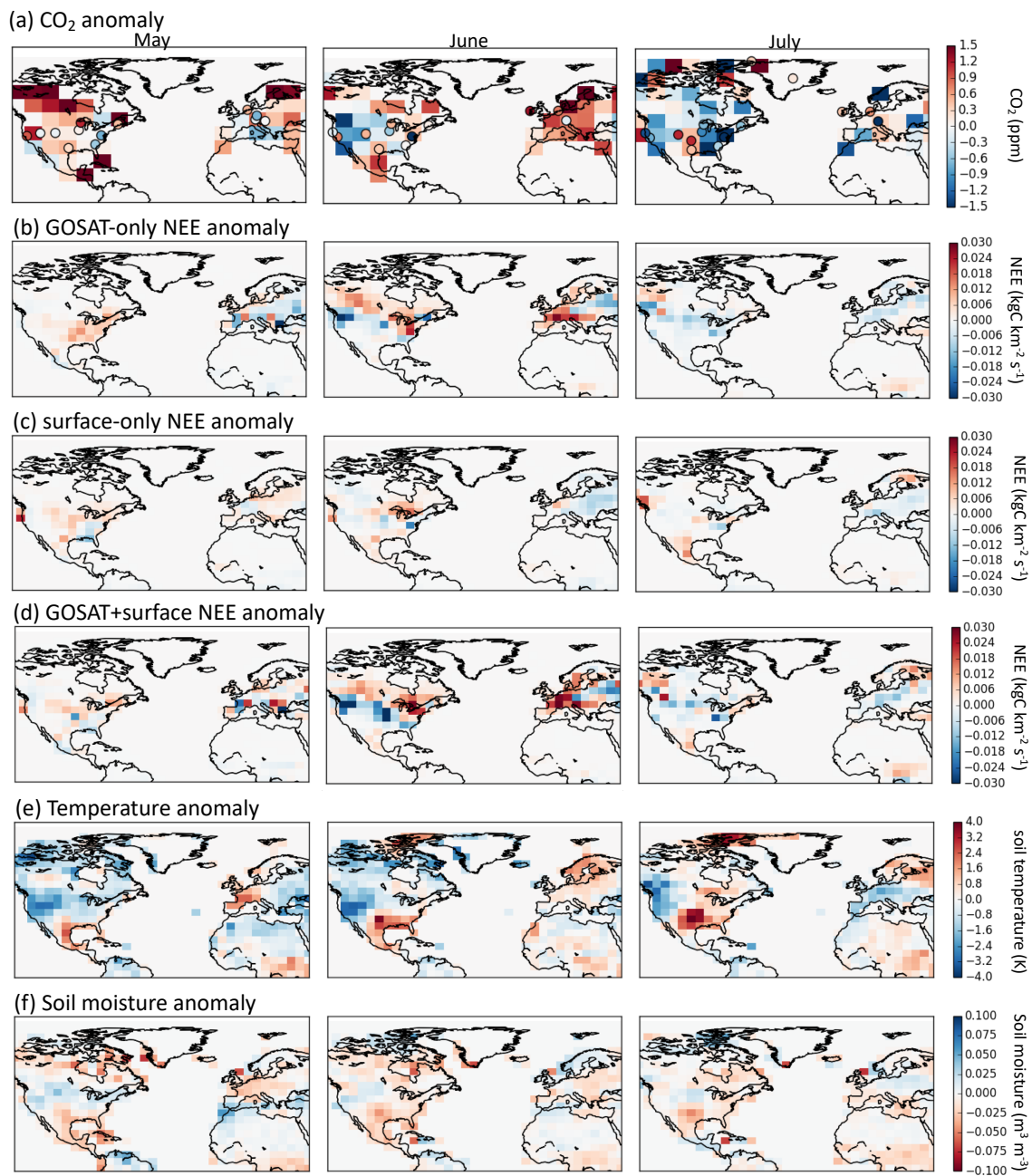


Figure 8. Monthly anomalies in (a) GOSAT X_{CO₂} (ppm, 4° × 5° grid cells) and surface site CO₂ (ppm divided by four, circles), (b) GOSAT-only posterior NEE, (c) surface-only posterior NEE, (d) GOSAT+surface posterior NEE, (e) MERRA-2 soil temperature, (f) ESA CCI soil moisture, for (left-to-right) May, June, and July of 2011.

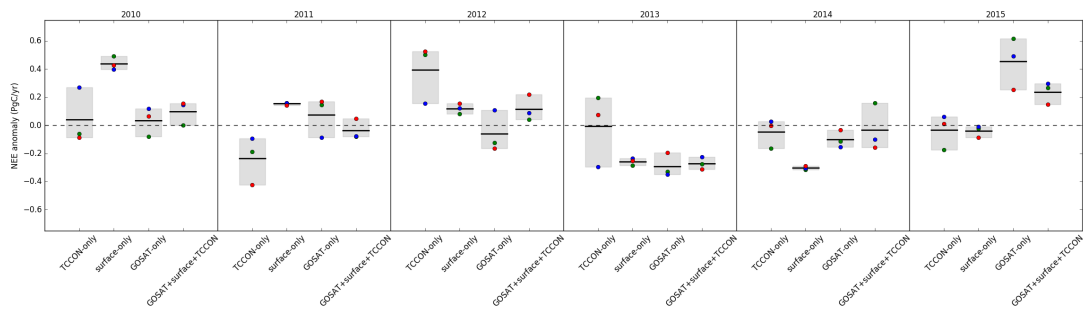


Figure 9. Annual net IAV in NEE over 2010-2015 for the TCCON-only, surface-only, GOSAT-only, and GOSAT+surface+TCCON flux inversions. Shaded grey regions show the range for the fluxes, while the solid black line shows the mean. Individual inversions are shown by the filled circles, with colors indicating prior NEE applied: green circles indicate SiB3, blue circles indicate CASA, and red circles indicate FLUXCOM.

523 not immediately clear, but could be due to advancements in the retrieval algorithm (e.g.,
 524 ACOS 3.3 and earlier versions were used in Houweling et al. (2015)) or due to the fact
 525 that we look at a multi-year mean while earlier studies looked at shorter time periods
 526 (e.g., Houweling et al. (2015) only examined June 2009 to June 2010). In fact, we find
 527 that the surface-only inversion suggests weaker uptake in 2010 than average (by 0.40 to
 528 0.49 PgC yr⁻¹), while the GOSAT flux inversion suggests near average uptake (see Sec. 4.3),
 529 suggesting that the difference in inferred fluxes between these two datasets may have been
 530 unusually large for 2010. However, it is important to note that differences in annual net
 531 fluxes do not imply biases in the measurements. There are aspects of the inversion set-
 532 ups that can lead to differences. For example, differences in the distribution of obser-
 533 vations can lead to significant differences in annual net fluxes (J. Liu et al., 2014; Byrne
 534 et al., 2017; Basu et al., 2018). Thus, one should not necessarily expect consistent annual
 535 net fluxes from observational datasets with spatial and temporal gaps in observa-
 536 tional coverage.

537 5.2 Does combining datasets improve flux inversions?

538 Is it possible to conclude that the GOSAT+surface+TCCON flux inversions im-
 539 prove flux estimates relative to the flux inversions that assimilate a single dataset? Of
 540 course, the answer to this question depends on how “improve” is defined. The GOSAT+surface+TCCON
 541 flux inversions generally show a small reduction in model-data differences against inde-
 542 pendent aircraft-based CO₂ and OCO-2 X_{CO₂} (north of 40°N). This suggests that combin-
 543 ing these datasets in a flux inversion framework produces NEE fluxes that better re-
 544 cover the true atmospheric CO₂ fields than any dataset alone. However, confounding fac-
 545 tors in evaluating these fluxes remain a significant concern. Model transport errors ap-
 546 pear to be a main driver of data-model differences for aircraft-based CO₂ measurements,
 547 and obscures the source of data-model differences. Evaluating optimized fluxes against
 548 OCO-2 is also problematic because these retrievals are known to have their own biases.

549 The GOSAT+surface+TCCON flux inversions improve the precision of the pos-
 550 terior NEE fluxes relative to the flux inversions assimilating one dataset. This is found
 551 to be the case at seasonal, annual, and interannual scales. The GOSAT+surface+TCCON
 552 flux inversions closely resemble the GOSAT-only NEE fluxes during the summer and surface-
 553 only fluxes during the winter for five northern extratropical regions. This is expected given
 554 the spatiotemporal distribution of GOSAT and surface-based CO₂ measurements and
 555 suggests that the GOSAT+surface+TCCON posterior NEE fluxes are better constrained

556 by the observations than the GOSAT-only or surface-only flux inversions. Therefore, the
 557 GOSAT+surface+TCCON flux inversions are less likely to be impacted by biases in the
 558 observational coverage, such that, from an observational coverage perspective, we can
 559 conclude that the GOSAT+surface+TCCON flux inversions are better constrained than
 560 the GOSAT-only or surface-only flux inversions.

561 An important concern in combining CO₂ datasets within a single flux inversion sys-
 562 tem is that there could be relative biases in the atmospheric CO₂ constraints provided
 563 by the different datasets. Any inconsistency in flux constraints between datasets has the
 564 potential of introducing artifacts into the posterior fluxes. Biases in the observations could
 565 be present due to errors in the X_{CO₂} retrieval algorithm, representativeness errors (Agustí-
 566 Panareda et al., 2019) or model transport errors. Several previous studies have suggested
 567 that unrealistically large uptake over Europe (~ 1.5 PgC yr⁻¹) is recovered in posterior
 568 fluxes due to biases in the GOSAT retrieval algorithm (Basu et al., 2013; Chevallier et
 569 al., 2014), although the ACOS retrieval algorithm has undergone significant development
 570 since these studies (Eldering et al., 2017; O’Dell et al., 2018) resulting in reduced biases
 571 (Miller & Michalak, 2019). Similarly, a number of studies have pointed out systematic
 572 transport errors in GEOS-Chem (Yu et al., 2018; Schuh et al., 2019), as-well as biases
 573 in reanalysis winds (e.g., vertical mixing, Parazoo et al. (2012)). We do not find clear
 574 evidence for biases between the surface-based and GOSAT constraints, although, these
 575 biases may be challenging to identify. However, we do see the impact of model transport
 576 errors in comparisons between the posterior-simulated-CO₂ and aircraft measurements.
 577 Ideally, this analysis should be performed with two different transport models so that
 578 transport related errors could be more easily identified.

579 6 Conclusions

580 This study presented a series of flux inversions assimilating surface-based flask and
 581 in situ CO₂ measurements, TCCON X_{CO₂}, GOSAT X_{CO₂}, or all datasets combined. All
 582 of the flux inversions showed improved agreement with independent aircraft-based CO₂
 583 measurements relative to prior flux estimates. The GOSAT+surface+TCCON flux in-
 584 version gave the smallest RMS differences against aircraft-based CO₂ measurements over
 585 East Asia and North America, and OCO-2 X_{CO₂} measurements (north of 40° N), sug-
 586 gesting that combining the datasets improves flux estimates. However, the data-model
 587 mismatches were strongly impacted by transport model, which makes robust evaluations
 588 of posterior surface fluxes challenging.

589 We found that all observing systems generally give consistent posterior NEE fluxes
 590 relative to the spread in prior fluxes. This suggests that these datasets provide consis-
 591 tent information on NEE. The GOSAT+surface+TCCON posterior NEE most closely
 592 resembles the GOSAT-only posterior NEE during the summer and surface-only poste-
 593 rior NEE during the winter, consistent with the temporal variations in the observational
 594 constraints. This suggests that the GOSAT+surface+TCCON flux inversions benefit from
 595 the improved spatiotemporal distribution of measurements, providing posterior fluxes
 596 that are better informed by measurements throughout the year.

597 The results of this study suggest that surface-based and space-based atmospheric
 598 CO₂ constraints provide consistent constraints on NEE fluxes, and can be combined in
 599 a flux inversion framework. This result stands in contrast to earlier attempts to com-
 600 bine these datasets (Houweling et al., 2015), and suggests that the improved consistency
 601 between the datasets has been made possible by the considerable effort spent refining
 602 the ACOS retrieval algorithm (Eldering et al., 2017; O’Dell et al., 2018; Kiel et al., 2019;
 603 Chevallier et al., 2019; Miller & Michalak, 2019).

7 Appendix: Prior NEE fluxes and errors

7.1 Simple biosphere model (SiB3)

SiB3 was originally designed as a lower boundary for General Circulation Models with explicit treatment of biophysical processes. The ability to ingest satellite phenology was later introduced (P. Sellers et al., 1996; P. J. Sellers et al., 1996), and further refinements included a prognostic canopy air space (Vidale & Stöckli, 2005), more realistic soil and snow (I. Baker et al., 2003) and modifications to calculations of root water uptake and soil water stress (I. Baker et al., 2008). The current version is called SiB3. Simulations used in this analysis use phenology (Leaf Area Index, LAI; fraction of Photosynthetically Active Radiation, fPAR) from the Moderate Resolution Imaging Spectroradiometer (MODIS). MERRA reanalysis is used as model inputs, with precipitation scaled to Global Precipitation Climatology Project (GPCP: Adler et al. (2003)) following I. T. Baker et al. (2010).

These fluxes are adjusted to obtain a global net drawdown equal to 4.6 PgC yr^{-1} . To do this, the annual net flux at each grid cell and global total annual net drawdown are calculated. The annual net flux at each gridcell is then scaled so that the annual net flux is 4.6 PgC yr^{-1} . The difference between the original and scaled annual net flux at each grid cell is then calculated. From this difference, an adjustment at each grid cell for each 14-day period is performed so that the annual net flux then equals the scaled annual net flux at each grid cell.

The prior NEE errors are generated based on the NEE fluxes provided by the models. It is first taken to be 60% of the NEE flux. This is then increased by scaling up the errors if the mean flux for a given gridcell is large but the flux is small at a given time. For example, the uncertainty is scaled up during the fall. We also inflate the uncertainty where the flux is small for SiB3 but large for CASA and FLUXCOM. The final errors range from 100% to 500% of the NEE flux.

7.2 CASA

The version of the model used here, CASA-GFED3, was modified from Potter et al. (1993) as described in Randerson et al. (1996) and van der Werf et al. (2006). It is driven by MERRA reanalysis and satellite-observed NDVI to track plant phenology. We use the same fluxes as are used for the CarbonTracker 2016 (<https://www.esrl.noaa.gov/gmd/ccgg/carbontracker/>) prior. CASA outputs monthly fluxes of Net Primary Productivity (NPP) and heterotrophic respiration (R_H). From these fluxes, GPP and ecosystem respiration (R_e) are estimated to be $GPP = 2NPP$ and $R_e = R_H - NPP$. Temporal downscaling and smoothing was performed from monthly CASA fluxes to 90-min fluxes using temperature and shortwave radiation from the ECMWF ERA-interim reanalysis (note this method differs from Olsen and Randerson (2004)). GFED.CMS is used for global fire emissions (<http://nacp-files.nacarbon.org/nacp-kawa-01/>). We use average model fluxes by averaging the fluxes for 2007–2012.

These fluxes are adjusted to obtain a global net drawdown equal to 4.6 PgC yr^{-1} . To do this, the annual net flux at each grid cell and global total annual net drawdown are calculated. The annual net flux at each gridcell is then scaled so that the annual net flux is 4.6 PgC yr^{-1} . The difference between the original and scaled annual net flux at each grid cell is then calculated. From this difference, an adjustment at each grid cell for each 14-day period is performed so that the annual net flux then equals the scaled annual net flux at each grid cell.

The prior NEE errors are generated based on the NEE fluxes provided by the models. It is first taken to be 60% of the NEE flux. This is then increased by scaling up the errors if the mean flux for a given gridcell is large but the flux is small at a given time. For example, the uncertainty is scaled up during the fall. We also inflate the uncertainty

653 where the flux is small for CASA but large for SiB3 and FLUXCOM. The final errors
 654 range from 100% to 500% of the NEE flux.

655 7.3 FLUXCOM

656 FLUXCOM products are generated using upscaling approaches based on machine
 657 learning methods that integrate FLUXNET site level observations, satellite remote sens-
 658 ing, and meteorological data (Tramontana et al., 2016; Jung et al., 2017). Jung et al.
 659 (2017) generate R_e products using several machine learning methods. For this study, we
 660 downloaded the products generated using random forests (RF), multivariate regression
 661 splines (MARS) and artificial neural networks (ANN) at daily resolution from the Data
 662 Portal of the Max Planck Institute for Biochemistry (<https://www.bgc-jena.mpg.de>). The
 663 mean seasonal cycle over 2008-2012 is calculated for each product.

664 These fluxes are adjusted to obtain a global net drawdown equal to 4.6 PgC yr^{-1} .
 665 For FLUXCOM, we only adjust fluxes south of 35° N because the northern extratrop-
 666 ical NEE fluxes have been heavily informed by FLUXNET sites. For grid cells south of
 667 35° N , the annual net flux at each grid cell and global total annual net drawdown are
 668 calculated. The annual net flux at each gridcell is then scaled so that the annual net flux
 669 is 4.6 PgC yr^{-1} . The difference between the original and scaled annual net flux at each
 670 grid cell is then calculated. From this difference, an adjustment at each grid cell for each
 671 14-day period is performed so that the annual net flux then equals the scaled annual net
 672 flux at each grid cell.

673 The prior NEE errors are generated based on the NEE fluxes provided by the mod-
 674 els. It is first taken to be 60% of the NEE flux. This is then increased by scaling up the
 675 errors if the mean flux for a given gridcell is large but the flux is small at a given time.
 676 For example, the uncertainty is scaled up during the fall. We also inflate the uncertainty
 677 where the flux is small for FLUXCOM but large for SiB3 and CASA. The final errors
 678 range from 100% to 500% of the NEE flux.

679 Acknowledgments

680 Brendan Byrne’s research was supported by an appointment to the NASA Postdoctoral
 681 Program at the Jet Propulsion Laboratory, administered by Universities Space Research
 682 Association under contract with NASA. The research carried out at the Jet Propulsion
 683 Laboratory, California Institute of Technology, was under a contract with the National
 684 Aeronautics and Space Administration. Kevin Bowman’s research was supported by the
 685 NASA Carbon Monitoring System (CMS) project (NNH16ZDA001N-CMS). Resources
 686 supporting this work were provided by the NASA High-End Computing (HEC) Program
 687 through the NASA Advanced Supercomputing (NAS) Division at Ames Research Cen-
 688 ter. The JR-STATION dataset is available from the Global Environmental Database,
 689 hosted by Center for Global Environmental Research (CGER), National Institute for En-
 690 vironmental Studies (NIES)

691 (<http://db.cger.nies.go.jp/portal/geds/atmosphericAndOceanicMonitoring>). TC-
 692 CON data were obtained from the TCCON Data Archive, hosted by CaltechDATA (<http://tccodata.org>).
 693 FLUXCOM products were obtained from the Data Portal of the Max Planck Institute
 694 for Biochemistry [<https://www.bgc-jena.mpg.de>]. MERRA-2 products were downloaded
 695 from MDISC [<https://gmao.gsfc.nasa.gov/reanalysis/MERRA-2/>], managed by the NASA
 696 Goddard Earth Sciences (GES) Data and Information Services Center (DISC). GOSAT
 697 OCFP v7.1 X_{CO_2} retrievals were downloaded from the Copernicus Climate Change Ser-
 698 vice website (<https://cds.climate.copernicus.eu>). Version 4.1 of the GLOBALVIEW plus
 699 package was downloaded from <http://www.esrl.noaa.gov/gmd/ccgg/obspack/>. ESA CCI
 700 soil moisture data was downloaded from <https://www.esa-soilmoisture-cci.org/>. Odiac
 701 emissions dataset was provided by T. Oda of Colorado State University, Fort Collins CO,
 702 USA/Global Monitoring Division, NOAA Earth System Research Laboratory, Boulder

703 CO, USA. Odiac project is supported by Greenhouse Gas Observing SATellite (GOSAT)
 704 project, National Institute for Environmental Studies (NIES), Japan. We thank S. Basu
 705 for providing downscaled ODIAC emissions. We thank T. Machida, H. Matsueda, Y. Sawa,
 706 and Y. Niwa for providing CONTRAIL measurements. The TCCON site at Réunion Is-
 707 land is operated by the Royal Belgian Institute for Space Aeronomy with financial sup-
 708 port in 2014, 2015, 2016, 2017, 2018 and 2019 under the EU project ICOS-Inwire and
 709 the ministerial decree for ICOS (FR/35/IC2) and local activities supported by LACy/UMR8105
 710 – Université de La Réunion. The TCCON project for Rikubetsu site is supported in part
 711 by the GOSAT series project. ©2019. All rights reserved.

712 **References**

713 Adler, R. F., Huffman, G. J., Chang, A., Ferraro, R., Xie, P.-P., Janowiak, J., ...
 714 others (2003). The version-2 Global Precipitation Climatology Project
 715 (GPCP) monthly precipitation analysis (1979–present). *J. Hydrometeorol.*,
 716 *4*(6), 1147–1167.

717 Agustí-Panareda, A., Diamantakis, M., Massart, S., Chevallier, F., Muñoz Sabater,
 718 J., Barré, J., ... Wunch, D. (2019). Modelling CO₂ weather – why hori-
 719 zontal resolution matters. *Atmos. Chem. Phys.*, *19*(11), 7347–7376. Re-
 720 trieved from <https://www.atmos-chem-phys.net/19/7347/2019/> doi:
 721 10.5194/acp-19-7347-2019

722 Bacastow, R. (1976). Modulation of atmospheric carbon dioxide by the southern os-
 723 cillation. *Nature*, *261*(5556), 116–118. doi: 10.1038/261116a0

724 Baker, I., Denning, A. S., Hanan, N., Prihodko, L., Uliasz, M., Vidale, P.-L., ...
 725 Bakwin, P. (2003). Simulated and observed fluxes of sensible and latent heat
 726 and CO₂ at the WLEF–TV tower using SiB2. 5. *Glob. Change Biol.*, *9*(9),
 727 1262–1277.

728 Baker, I., Prihodko, L., Denning, A., Goulden, M., Miller, S., & Da Rocha, H.
 729 (2008). Seasonal drought stress in the Amazon: Reconciling models and obser-
 730 vations. *J. Geophys. Res.-Biogeo.*, *113*(G00B01). doi: 10.1029/2007JG000644

731 Baker, I. T., Denning, A. S., & Stöckli, R. (2010). North American gross primary
 732 productivity: regional characterization and interannual variability. *Tellus B*,
 733 *62*(5), 533–549. doi: 10.1111/j.1600-0889.2010.00492.x

734 Basu, S., Baker, D. F., Chevallier, F., Patra, P. K., Liu, J., & Miller, J. B. (2018).
 735 The impact of transport model differences on co₂ surface flux estimates from
 736 oco-2 retrievals of column average co₂. *Atmospheric Chemistry & Physics*,
 737 *18*(10).

738 Basu, S., Guerlet, S., Butz, A., Houweling, S., Hasekamp, O., Aben, I., ... oth-
 739 ers (2013). Global CO₂ fluxes estimated from GOSAT retrievals of to-
 740 tal column CO₂. *Atmos. Chem. Phys.*, *13*(17), 8695–8717. doi: 10.5194/
 741 acp-13-8695-2013

742 Bolin, B., & Keeling, C. (1963). Large-scale atmospheric mixing as deduced from the
 743 seasonal and meridional variations of carbon dioxide. *J. Geophys. Res.*, *68*(13),
 744 3899–3920. doi: 0.1029/JZ068i013p03899

745 Bowman, K., Liu, J., Bloom, A., Parazoo, N., Lee, M., Jiang, Z., ... others (2017).
 746 Global and Brazilian carbon response to El Niño Modoki 2011–2010. *Earth
 747 and Space Sci.*, *4*(10), 637–660. doi: 10.1002/2016EA000204

748 Brix, H., Menemenlis, D., Hill, C., Dutkiewicz, S., Jahn, O., Wang, D., ... Zhang,
 749 H. (2015). Using green’s functions to initialize and adjust a global, eddy
 750 ocean biogeochemistry general circulation model. *Ocean Modelling*, *95*, 1–14.

751 Bruhwiler, L., Michalak, A., & Tans, P. (2011). Spatial and temporal resolution of
 752 carbon flux estimates for 1983–2002. *Biogeosciences*, *8*(5), 1309–1331. doi: 10
 753 .5194/bg-8-1309-2011

754 Byrne, B., Jones, D. B. A., Strong, K., Polavarapu, S. M., Harper, A. B., Baker,
 755 D. F., & Maksyutov, S. (2019). On what scales can gosat flux inversions

- 756 constrain anomalies in terrestrial ecosystems? *Atmos. Chem. Phys.*, *19*(20),
 757 13017–13035. doi: 10.5194/acp-19-13017-2019
- 758 Byrne, B., Jones, D. B. A., Strong, K., Zeng, Z.-C., Deng, F., & Liu, J. (2017). Sen-
 759 sitivity of CO₂ surface flux constraints to observational coverage. *J. Geophys.*
 760 *Res.-Atmos*, *112*(12), 6672–6694. doi: 10.1002/2016JD026164
- 761 Byrne, B., Wunch, D., Jones, D., Strong, K., Deng, F., Baker, I., . . . others (2018).
 762 Evaluating GPP and respiration estimates over northern midlatitude ecosys-
 763 tems using solar-induced fluorescence and atmospheric CO₂ measurements.
 764 *Journal of Geophysical Research: Biogeosciences*, *123*(9), 2976–2997.
- 765 Chatterjee, A., Gierach, M., Sutton, A., Feely, R., Crisp, D., Eldering, A., . . .
 766 Schimel, D. (2017). Influence of El Niño on atmospheric CO₂ over the tropical
 767 Pacific Ocean: Findings from NASA’s OCO-2 mission. *Science*, *358*(6360),
 768 eaam5776. doi: 10.1126/science.aam5776
- 769 Chevallier, F., Deutscher, N. M., Conway, T., Ciais, P., Ciattaglia, L., Dohe, S., . . .
 770 others (2011). Global CO₂ fluxes inferred from surface air-sample measure-
 771 ments and from TCCON retrievals of the CO₂ total column. *Geophys. Res.*
 772 *Lett.*, *38*(24).
- 773 Chevallier, F., Palmer, P. I., Feng, L., Boesch, H., O’Dell, C. W., & Bousquet, P.
 774 (2014). Toward robust and consistent regional CO₂ flux estimates from in situ
 775 and spaceborne measurements of atmospheric CO₂. *Geophys. Res. Lett.*, *41*(3),
 776 1065–1070. (2013GL058772) doi: 10.1002/2013GL058772
- 777 Chevallier, F., Remaud, M., O’Dell, C. W., Baker, D., Peylin, P., & Cozic,
 778 A. (2019). Objective evaluation of surface- and satellite-driven CO₂ at-
 779 mospheric inversions. *Atmos. Chem. Phys. Discuss.*, *2019*, 1–28. doi:
 780 10.5194/acp-2019-213
- 781 Cooperative Global Atmospheric Data Integration Project. (2018). *Multi-laboratory*
 782 *compilation of atmospheric carbon dioxide data for the period 1957-2017;*
 783 *obspack_CO2_1_globalviewplus_v4.1.2018.10.29; noaa earth system research*
 784 *laboratory, global monitoring division.* doi: 10.25925/20181026
- 785 Crisp, D., Atlas, R., Breon, F.-M., Brown, L., Burrows, J., Ciais, P., . . . others
 786 (2004). The orbiting carbon observatory (OCO) mission. *Advances in Space*
 787 *Research*, *34*(4), 700–709.
- 788 Crisp, D., Fisher, B. M., O’Dell, C., Frankenberg, C., Basilio, R., Bösch, H., . . .
 789 Yung, Y. L. (2012). The ACOS CO₂ retrieval algorithm-Part II: Global
 790 XCO₂ data characterization. *Atmos. Meas. Tech.*, *5*(4), 687–707. doi:
 791 10.5194/amt-5-687-2012
- 792 De Mazière, M., Sha, M. K., Desmet, F., Hermans, C., Scolas, F., Kumps, N.,
 793 . . . Cammas, J.-P. (2017). *Tcon data from réunion island (re), release*
 794 *ggg2014.r1.* CaltechDATA. Retrieved from [https://data.caltech.edu/](https://data.caltech.edu/records/322)
 795 [records/322](https://data.caltech.edu/records/322) doi: 10.14291/tcon.ggg2014.reunion01.r1
- 796 Diallo, M., Legras, B., Ray, E., Engel, A., & Añel, J. A. (2017). Global distribu-
 797 tion of CO₂ in the upper troposphere and stratosphere. *Atmos. Chem. Phys.*,
 798 *17*(6), 3861–3878. Retrieved from [https://www.atmos-chem-phys.net/17/](https://www.atmos-chem-phys.net/17/3861/2017/)
 799 [3861/2017/](https://www.atmos-chem-phys.net/17/3861/2017/) doi: 10.5194/acp-17-3861-2017
- 800 Dorigo, W., Wagner, W., Albergel, C., Albrecht, F., Balsamo, G., Brocca, L., . . .
 801 others (2017). Esa cci soil moisture for improved earth system understanding:
 802 State-of-the art and future directions. *Remote Sens. Environ.*, *203*, 185–215.
- 803 Dutkiewicz, S., Follows, M. J., & Bragg, J. G. (2009). Modeling the coupling of
 804 ocean ecology and biogeochemistry. *Global Biogeochem. Cy.*, *23*(4).
- 805 Eldering, A., O’Dell, C. W., Wennberg, P. O., Crisp, D., Gunson, M. R., Viatte,
 806 C., . . . Yoshimizu, J. (2017). The orbiting carbon observatory-2: first
 807 18 months of science data products. *Atmos. Meas. Tech.*, *10*(2), 549–563.
 808 doi: 10.5194/amt-10-549-2017
- 809 Feist, D. G., Arnold, S. G., John, N., & Geibel, M. C. (2017). *Tcon data*
 810 *from ascension island (sh), release ggg2014.r0.* CaltechDATA. Re-

811 trieved from <https://data.caltech.edu/records/210> doi: 10.14291/
812 tccon.ggg2014.ascension01.r0/1149285

813 Fischer, M. L., Parazoo, N., Brophy, K., Cui, X., Jeong, S., Liu, J., ... others
814 (2017). Simulating estimation of california fossil fuel and biosphere carbon
815 dioxide exchanges combining in situ tower and satellite column observations. *J.*
816 *Geophys. Res.-Atmos.*, *122*(6), 3653–3671.

817 Gelaro, R., McCarty, W., Suárez, M. J., Todling, R., Molod, A., Takacs, L., ...
818 others (2017). The modern-era retrospective analysis for research and applica-
819 tions, version 2 (MERRA-2). *J. Climate*, *30*(14), 5419–5454.

820 Griffith, D. W., Deutscher, N. M., Velazco, V. A., Wennberg, P. O., Yavin, Y.,
821 Keppel-Aleks, G., ... Bryant, G. W. (2017). *Tccon data from darwin (au), re-*
822 *lease ggg2014.r0*. CaltechDATA. Retrieved from [https://data.caltech.edu/](https://data.caltech.edu/records/269)
823 [records/269](https://data.caltech.edu/records/269) doi: 10.14291/tccon.ggg2014.darwin01.r0/1149290

824 Griffith, D. W., Velazco, V. A., Deutscher, N. M., Paton-Walsh, C., Jones, N. B.,
825 Wilson, S. R., ... Riggenbach, M. O. (2017). *Tccon data from wollongong*
826 *(au), release ggg2014.r0*. CaltechDATA. Retrieved from [https://data](https://data.caltech.edu/records/291)
827 [.caltech.edu/records/291](https://data.caltech.edu/records/291) doi: 10.14291/tccon.ggg2014.wollongong01.r0/
828 1149291

829 Gruber, A., Dorigo, W. A., Crow, W., & Wagner, W. (2017). Triple collocation-
830 based merging of satellite soil moisture retrievals. *IEEE T. Geosci. Remote*,
831 *55*(12), 6780–6792.

832 Gurney, K. R., Baker, D., Rayner, P., & Denning, S. (2008). Interannual varia-
833 tions in continental-scale net carbon exchange and sensitivity to observing
834 networks estimated from atmospheric CO₂ inversions for the period 1980 to
835 2005. *Global Biogeochem. Cy.*, *22*(3). Retrieved from [http://dx.doi.org/](http://dx.doi.org/10.1029/2007GB003082)
836 [10.1029/2007GB003082](http://dx.doi.org/10.1029/2007GB003082) (GB3025) doi: 10.1029/2007GB003082

837 Houweling, S., Baker, D., Basu, S., Boesch, H., Butz, A., Chevallier, F., ... oth-
838 ers (2015). An intercomparison of inverse models for estimating sources and
839 sinks of CO₂ using GOSAT measurements. *J. Geophys. Res.-Atmos.*, *120*(10),
840 5253–5266.

841 ICOS RI. (2019). *Icos atmospheric greenhouse gas mole fractions of CO₂, CH₄,*
842 *CO, ¹⁴CO₂ and meteorological observations september 2015 - april 2019 for 19*
843 *stations (49 vertical levels), final quality controlled level 2 data (version 1.0).*
844 *icos eric - carbon portal*. doi: 10.18160/CE2R-CC91

845 Iraci, L. T., Podolske, J. R., Hillyard, P. W., Roehl, C., Wennberg, P. O., Blavier,
846 J.-F., ... Boyden, H. (2017). *Tccon data from edwards (us), release*
847 *ggg2014.r1*. CaltechDATA. Retrieved from [https://data.caltech.edu/](https://data.caltech.edu/records/270)
848 [records/270](https://data.caltech.edu/records/270) doi: 10.14291/tccon.ggg2014.edwards01.r1/1255068

849 Jung, M., Reichstein, M., Schwalm, C. R., Huntingford, C., Sitch, S., Ahlström, A.,
850 ... others (2017). Compensatory water effects link yearly global land CO₂ sink
851 changes to temperature. *Nature*, *541*(7638), 516–520.

852 Keeling, C. D. (1960). The concentration and isotopic abundances of carbon dioxide
853 in the atmosphere. *Tellus*, *12*(2), 200–203.

854 Keeling, C. D., Chin, J., & Whorf, T. (1996). Increased activity of northern vege-
855 tation inferred from atmospheric CO₂ measurements. *Nature*, *382*(6587), 146-
856 149.

857 Kiel, M., O'Dell, C. W., Fisher, B., Eldering, A., Nassar, R., MacDonald, C. G., &
858 Wennberg, P. O. (2019). How bias correction goes wrong: measurement of
859 xco2 affected by erroneous surface pressure estimates. *Atmos. Meas. Tech.*,
860 *12*(4).

861 Liu, J., Bowman, K. W., Lee, M., Henze, D. K., Bousserrez, N., Brix, H., ... others
862 (2014). Carbon monitoring system flux estimation and attribution: impact
863 of ACOS-GOSAT XCO₂ sampling on the inference of terrestrial biospheric
864 sources and sinks. *Tellus B*, *66*(1), 22486. doi: 10.3402/tellusb.v66.22486

865 Liu, J., Bowman, K. W., Schimel, D. S., Parazoo, N. C., Jiang, Z., Lee, M., ... El-

- 866 dering, A. (2017). Contrasting carbon cycle responses of the tropical continents
 867 to the 2015–2016 el niño. *Science*, *358*(6360). doi: 10.1126/science.aam5690
- 868 Liu, Y. Y., Dorigo, W. A., Parinussa, R., de Jeu, R. A., Wagner, W., McCabe,
 869 M. F., ... Van Dijk, A. (2012). Trend-preserving blending of passive and ac-
 870 tive microwave soil moisture retrievals. *Remote Sens. Environ.*, *123*, 280–297.
- 871 Liu, Y. Y., Parinussa, R., Dorigo, W. A., De Jeu, R. A., Wagner, W., Van Dijk, A.,
 872 ... Evans, J. (2011). Developing an improved soil moisture dataset by blend-
 873 ing passive and active microwave satellite-based retrievals. *Hydrol. Earth Syst.*
 874 *Sc.*, *15*(2), 425–436.
- 875 Machida, T., Matsueda, H., Sawa, Y., Nakagawa, Y., Hirokuni, K., Kondo, N., ...
 876 Ogawa, T. (2008). Worldwide measurements of atmospheric CO₂ and other
 877 trace gas species using commercial airlines. *Journal of Atmospheric and*
 878 *Oceanic Technology*, *25*(10), 1744–1754.
- 879 Machida, T., Matsueda, H., Sawa, Y., & Niwa, Y. (2018). *Atmospheric CO₂ mole*
 880 *fraction data of CONTRAIL-CME, Ver.2017.1.0, center for global envi-*
 881 *ronmental research, NIES (reference date: 2018/11/28)*. doi: 10.17595/
 882 20180208.001
- 883 Masarie, K., Peters, W., Jacobson, A., & Tans, P. (2014). Obspack: a framework
 884 for the preparation, delivery, and attribution of atmospheric greenhouse gas
 885 measurements. *Earth Syst. Sci. Data*, *6*(2), 375–384.
- 886 Menemenlis, D., Campin, J.-M., Heimbach, P., Hill, C., Lee, T., Nguyen, A., ...
 887 Zhang, H. (2008). Ecco2: High resolution global ocean and sea ice data syn-
 888 thesis. *Mercator Ocean Quarterly Newsletter*, *31*(October), 13–21.
- 889 Miller, S. M., & Michalak, A. M. (2019). The impact of improved satellite retrievals
 890 on estimates of biospheric carbon balance. *Atmos. Chem. Phys. Discuss.*,
 891 *2019*, 1–15. Retrieved from [https://www.atmos-chem-phys-discuss.net/](https://www.atmos-chem-phys-discuss.net/acp-2019-382/)
 892 [acp-2019-382/](https://www.atmos-chem-phys-discuss.net/acp-2019-382/) doi: 10.5194/acp-2019-382
- 893 Morino, I., Yokozeki, N., Matsuzaki, T., & Horikawa, M. (2017). *Tcccon data*
 894 *from rikubetsu (jp), release ggg2014.r2*. CaltechDATA. Retrieved from
 895 <https://data.caltech.edu/records/957> doi: 10.14291/tccon.ggg2014
 896 .rikubetsu01.r2
- 897 Nassar, R., Napier-Linton, L., Gurney, K. R., Andres, R. J., Oda, T., Vogel, F. R.,
 898 & Deng, F. (2013). Improving the temporal and spatial distribution of CO₂
 899 emissions from global fossil fuel emission data sets. *J. Geophys. Res.-Atmos.*,
 900 *118*(2), 917–933.
- 901 Nassar, R., Sioris, C. E., Jones, D., & McConnell, J. C. (2014). Satellite observa-
 902 tions of CO₂ from a highly elliptical orbit for studies of the Arctic and boreal
 903 carbon cycle. *J. Geophys. Res.-Atmos.*, *119*(5), 2654–2673.
- 904 Nelson, R. R., & O’Dell, C. W. (2019). The impact of improved aerosol priors on
 905 near-infrared measurements of carbon dioxide. *Atmos. Meas. Tech.*, *12*(3),
 906 1495–1512. Retrieved from [https://www.atmos-meas-tech.net/12/1495/](https://www.atmos-meas-tech.net/12/1495/2019/)
 907 [2019/](https://www.atmos-meas-tech.net/12/1495/2019/) doi: 10.5194/amt-12-1495-2019
- 908 Oda, T., & Maksyutov, S. (2011). A very high-resolution (1 km × 1 km) global fossil
 909 fuel CO₂ emission inventory derived using a point source database and satellite
 910 observations of nighttime lights. *Atmos. Chem. Phys.*, *11*(2), 543–556.
- 911 Oda, T., Maksyutov, S., & Andres, R. J. (2018). The open-source data inven-
 912 tory for anthropogenic CO₂, version 2016 (odiac2016): a global monthly fos-
 913 sil fuel CO₂ gridded emissions data product for tracer transport simulations
 914 and surface flux inversions. *Earth Syst. Sci. Data*, *10*(1), 87–107. Re-
 915 trieved from <https://www.earth-syst-sci-data.net/10/87/2018/> doi:
 916 10.5194/essd-10-87-2018
- 917 O’Dell, C. W., Connor, B., Bösch, H., O’Brien, D., Frankenberg, C., Castano, R., ...
 918 Wunch, D. (2012). The ACOS CO₂ retrieval algorithm – part 1: Description
 919 and validation against synthetic observations. *Atmos. Meas. Tech.*, *5*(1), 99–
 920 121. Retrieved from <http://www.atmos-meas-tech.net/5/99/2012/> doi:

- 10.5194/amt-5-99-2012
- O'Dell, C. W., Eldering, A., Wennberg, P. O., Crisp, D., Gunson, M. R., Fisher, B., ... Velasco, V. A. (2018). Improved retrievals of carbon dioxide from orbiting carbon observatory-2 with the version 8 acos algorithm. *Atmos. Meas. Tech.*, *11*(12), 6539–6576. Retrieved from <https://www.atmos-meas-tech.net/11/6539/2018/> doi: 10.5194/amt-11-6539-2018
- Olsen, S. C., & Randerson, J. T. (2004). Differences between surface and column atmospheric CO₂ and implications for carbon cycle research. *J. Geophys. Res.-Atmos.*, *109*(D2). (D02301) doi: 10.1029/2003JD003968
- Parazoo, N. C., Denning, A. S., Kawa, S. R., Pawson, S., & Lokupitiya, R. (2012). CO₂ flux estimation errors associated with moist atmospheric processes. *Atmos. Chem. Phys.*, *12*(14), 6405–6416. doi: 10.5194/acp-12-6405-2012
- Philip, S., Johnson, M. S., Potter, C., Genovesse, V., Baker, D. F., Haynes, K. D., ... Poulter, B. (2019). Prior biosphere model impact on global terrestrial CO₂ fluxes estimated from oco-2 retrievals. *Atmos. Chem. Phys. Discuss.*, *2019*, 1–29. doi: 10.5194/acp-2018-1095
- Polavarapu, S. M., Deng, F., Byrne, B., Jones, D. B. A., & Neish, M. (2018). A comparison of posterior atmospheric CO₂ adjustments obtained from in situ and gosat constrained flux inversions. *Atmos. Chem. Phys.*, *18*(16), 12011–12044. doi: 10.5194/acp-18-12011-2018
- Randerson, J. T., Thompson, M. V., Malmstrom, C. M., Field, C. B., & Fung, I. Y. (1996). Substrate limitations for heterotrophs: Implications for models that estimate the seasonal cycle of atmospheric CO₂. *Global Biogeochem. Cy.*, *10*(4), 585–602. doi: 10.1029/96GB01981
- Randerson, J. T., Van Der Werf, G., Giglio, L., Collatz, G., & Kasibhatla, P. (2018). Global fire emissions database, version 4.1 (gfedv4). *ORNL DAAC*. doi: 10.3334/ORNLDAAC/1293
- Reichle, R. H., Draper, C. S., Liu, Q., Girotto, M., Mahanama, S. P., Koster, R. D., & De Lannoy, G. J. (2017). Assessment of MERRA-2 land surface hydrology estimates. *J. Climate*, *30*(8), 2937–2960.
- Reichle, R. H., Koster, R. D., De Lannoy, G. J., Forman, B. A., Liu, Q., Mahanama, S. P., & Touré, A. (2011). Assessment and enhancement of MERRA land surface hydrology estimates. *J. Climate*, *24*(24), 6322–6338.
- Reuter, M., Buchwitz, M., Hilker, M., Heymann, J., Schneising, O., Pillai, D., ... others (2014). Satellite-inferred european carbon sink larger than expected. *Atmos. Chem. Phys.*, *14*(24), 13739–13753.
- Rödenbeck, C., Houweling, S., Gloor, M., & Heimann, M. (2003). CO₂ flux history 1982–2001 inferred from atmospheric data using a global inversion of atmospheric transport. *Atmos. Chem. Phys.*, *3*(6), 1919–1964.
- Saeki, T., Maksyutov, S., Saito, M., Valsala, V., Oda, T., RJ, A., ... others (2013). Inverse modeling of CO₂ fluxes using gosat data and multi-year ground-based observations. *Sola*, *9*, 45–50.
- Sasakawa, M., Machida, T., Tsuda, N., Arshinov, M., Davydov, D., Fofonov, A., & Krasnov, O. (2013). Aircraft and tower measurements of CO₂ concentration in the planetary boundary layer and the lower free troposphere over southern taiga in West Siberia: Long-term records from 2002 to 2011. *J. Geophys. Res.-Atmos.*, *118*(16), 9489–9498. doi: 10.1002/jgrd.50755
- Sasakawa, M., Shimoyama, K., Machida, T., Tsuda, N., Suto, H., Arshinov, M., ... others (2010). Continuous measurements of methane from a tower network over Siberia. *Tellus B*, *62*(5), 403–416. doi: 10.1111/j.1600-0889.2010.00494.x
- Schuh, A. E., Jacobson, A. R., Basu, S., Weir, B., Baker, D., Bowman, K., ... others (2019). Quantifying the impact of atmospheric transport uncertainty on co2 surface flux estimates. *Global Biogeochem. Cy.*, *33*(4), 484–500.
- Sellers, P., Randall, D., Collatz, G., Berry, J., Field, C., Dazlich, D., ... Bounoua, L. (1996). A revised land surface parameterization (SiB2) for atmospheric GCMs.

- 976 part I: Model formulation. *J. Climate*, 9(4), 676–705.
- 977 Sellers, P. J., Tucker, C. J., Collatz, G. J., Los, S. O., Justice, C. O., Dazlich, D. A.,
978 & Randall, D. A. (1996). A revised land surface parameterization (SiB2)
979 for atmospheric GCMs. part II: The generation of global fields of terrestrial
980 biophysical parameters from satellite data. *J. Climate*, 9(4), 706–737.
- 981 Strong, K., Roche, S., Franklin, J. E., Mendonca, J., Lutsch, E., Weaver, D., ...
982 Lindenmaier, R. (2017). *Tcccon data from eureka (ca), release ggg2014.r2*. Cal-
983 techDATA. Retrieved from <https://data.caltech.edu/records/970> doi:
984 10.14291/tcccon.ggg2014.eureka01.r2
- 985 Sweeney, C., Karion, A., Wolter, S., Newberger, T., Guenther, D., Higgs, J. A., ...
986 others (2015). Seasonal climatology of CO₂ across North America from air-
987 craft measurements in the NOAA/ESRL Global Greenhouse Gas Reference
988 Network. *J. Geophys. Res.-Atmos.*, 120(10), 5155–5190.
- 989 Tans, P. P., Conway, T. J., & Nakazawa, T. (1989). Latitudinal distribution of the
990 sources and sinks of atmospheric carbon dioxide derived from surface observa-
991 tions and an atmospheric transport model. *J. Geophys. Res.-Atmos.*, 94(D4),
992 5151–5172.
- 993 Tramontana, G., Jung, M., Schwalm, C. R., Ichii, K., Camps-Valls, G., Ráduly, B.,
994 ... Papale, D. (2016). Predicting carbon dioxide and energy fluxes across
995 global FLUXNET sites with regression algorithms. *Biogeosciences*, 13(14),
996 4291–4313. doi: 10.5194/bg-13-4291-2016
- 997 van der Werf, G. R., Randerson, J. T., Giglio, L., Collatz, G. J., Kasibhatla, P. S.,
998 & Arellano Jr, A. F. (2006). Interannual variability in global biomass burning
999 emissions from 1997 to 2004. *Atmos. Chem. Phys.*, 6(11), 3423–3441.
- 1000 Vidale, P., & Stöckli, R. (2005). Prognostic canopy air space solutions for land sur-
1001 face exchanges. *Theor. Appl. Climatol.*, 80(2-4), 245–257.
- 1002 Wagner, W., Dorigo, W., de Jeu, R., Fernandez, D., Benveniste, J., Haas, E., ...
1003 others (2012). Fusion of active and passive microwave observations to create
1004 an essential climate variable data record on soil moisture. *ISPRS Annals of the*
1005 *Photogrammetry, Remote Sensing and Spatial Information Sciences (ISPRS*
1006 *Annals)*, 7, 315–321.
- 1007 Wang, J. S., Kawa, S. R., Collatz, G. J., Sasakawa, M., Gatti, L. V., Machida, T.,
1008 ... Manyin, M. E. (2018). A global synthesis inversion analysis of recent vari-
1009 ability in CO₂ fluxes using gosat and in situ observations. *Atmos. Chem. Phys.*,
1010 18(15), 11097–11124. Retrieved from [https://www.atmos-chem-phys.net/](https://www.atmos-chem-phys.net/18/11097/2018/)
1011 18/11097/2018/ doi: 10.5194/acp-18-11097-2018
- 1012 Warneke, T., Messerschmidt, J., Notholt, J., Weinzierl, C., Deutscher, N. M., Petri,
1013 C., & Grupe, P. (2017). *Tcccon data from orléans (fr), release ggg2014.r0*. Cal-
1014 techDATA. Retrieved from <https://data.caltech.edu/records/283> doi:
1015 10.14291/tcccon.ggg2014.orleans01.r0/1149276
- 1016 Wennberg, P. O., Roehl, C. M., Wunch, D., Toon, G. C., Blavier, J.-F., Washen-
1017 felder, R., ... Ayers, J. (2017). *Tcccon data from park falls (us), release*
1018 *ggg2014.r1*. CaltechDATA. Retrieved from [https://data.caltech.edu/](https://data.caltech.edu/records/295)
1019 [records/295](https://data.caltech.edu/records/295) doi: 10.14291/tcccon.ggg2014.parkfalls01.r1
- 1020 Wennberg, P. O., Wunch, D., Roehl, C. M., Blavier, J.-F., Toon, G. C., & Allen,
1021 N. T. (2017). *Tcccon data from lamont (us), release ggg2014.r1*. Caltech-
1022 DATA. Retrieved from <https://data.caltech.edu/records/279> doi:
1023 10.14291/tcccon.ggg2014.lamont01.r1/1255070
- 1024 Wofsy, S. C. (2011). HIAPER pole-to-pole observations (HIPPO): fine-grained,
1025 global-scale measurements of climatically important atmospheric gases and
1026 aerosols. *Philos. T. R. Soc. A.*, 369(1943), 2073–2086.
- 1027 Wunch, D., Toon, G. C., Blavier, J.-F. L., Washenfelder, R. A., Notholt, J., Con-
1028 nor, B. J., ... Wennberg, P. O. (2011). The Total Carbon Column Ob-
1029 serving Network. *Philos. T. Roy. Soc. A*, 369(1943), 2087–2112. doi:
1030 10.1098/rsta.2010.0240

1031 Wunch, D., Toon, G. C., Wennberg, P. O., Wofsy, S. C., Stephens, B. B., Fischer,
 1032 M. L., ... Zondlo, M. A. (2010). Calibration of the total carbon column
 1033 observing network using aircraft profile data. *Atmos. Meas. Tech.*, *3*(5), 1351–
 1034 1362. doi: 10.5194/amt-3-1351-2010

1035 Yokota, T., Yoshida, Y., Eguchi, N., Ota, Y., Tanaka, T., Watanabe, H., & Maksyu-
 1036 tov, S. (2009). Global concentrations of co2 and ch4 retrieved from gosat:
 1037 First preliminary results. *Sola*, *5*, 160–163.

1038 Yoshida, Y., Kikuchi, N., Morino, I., Uchino, O., Oshchepkov, S., Bril, A., ... others
 1039 (2013). Improvement of the retrieval algorithm for GOSAT SWIR XCO₂ and
 1040 XCH₄ and their validation using TCCON data.

1041 Yu, K., Keller, C. A., Jacob, D. J., Molod, A. M., Eastham, S. D., & Long, M. S.
 1042 (2018). Errors and improvements in the use of archived meteorological
 1043 data for chemical transport modeling: an analysis using GEOS-Chem v11-
 1044 01 driven by GEOS-5 meteorology. *Geosci. Model Dev.*, *11*(1), 305–319. doi:
 1045 10.5194/gmd-11-305-2018